

Fate induction in CD8 CAR T cells through asymmetric cell division

<https://doi.org/10.1038/s41586-024-07862-7>

Received: 29 September 2022

Accepted: 22 July 2024

Published online: 28 August 2024

Open access

 Check for updates

Casey S. Lee^{1,2,6}, Sisi Chen^{1,2,6}, Corbett T. Berry^{1,2}, Andre R. Kelly^{2,3}, Patrick J. Herman^{1,2}, Sangwook Oh⁴, Roddy S. O'Connor^{2,3}, Aimee S. Payne⁵✉ & Christoph T. Ellebrecht^{1,2}✉

Early expansion and long-term persistence predict efficacy of chimeric antigen receptor T cells (CARs)^{1–7}, but mechanisms governing effector versus memory CAR differentiation and whether asymmetric cell division induces differential fates in human CARs remain unclear. Here we show that target-induced proximity labelling enables isolation of first-division proximal-daughter and distal-daughter CD8 CARs that asymmetrically distribute their surface proteome and transcriptome, resulting in divergent fates. Target-engaged CARs remain on proximal daughters, which inherit a surface proteome resembling activated-undivided CARs, whereas the endogenous T cell receptor and CD8 enrich on distal daughters, whose surface proteome resembles resting CARs, correlating with glycolytic and oxidative metabolism, respectively. Despite memory-precursor phenotype and in vivo longevity, distal daughters demonstrate transient potent cytolytic activity similar to proximal daughters, uncovering an effector-like state in distal daughters destined to become memory CARs. Both partitioning of pre-existing transcripts and changes in RNA velocity contribute to asymmetry of fate-determining factors, resulting in diametrically opposed transcriptional trajectories. Independent of naive, memory or effector surface immunophenotype, proximal-daughter CARs use core sets of transcription factors known to support proliferation and effector function. Conversely, transcription factors enriched in distal daughters restrain differentiation and promote longevity, evidenced by diminished long-term in vivo persistence and function of distal-daughter CARs after *IKZF1* disruption. These studies establish asymmetric cell division as a framework for understanding mechanisms of CAR differentiation and improving therapeutic outcomes.

Long-term CAR persistence is associated with superior therapeutic outcome and is attributed to the formation of long-lived memory CARs that afford continuous immunosurveillance to prevent cancer recurrence^{1–7}. In mouse models of infection and ovalbumin immunization, asymmetric cell division (ACD) has been observed as one mechanism of memory formation after CD8 T cell activation^{8–11}. The daughter cell proximal to the antigen presenting cell inherits the immunologic synapse, shows a moderate increase in CD8 surface expression⁸ and is more likely to differentiate into a short-lived effector T (T_{eff}) cell. The distal-daughter cell, conversely, becomes a long-lived memory cell with distinct transcriptional¹², epigenetic¹³ and metabolic profile⁹. Despite considerable interest in CAR phenotypes and memory formation over the past decade, the cellular mechanisms underlying the development of long- or short-lived CARs and specifically whether ACD has a role in this process, remain unclear. Whereas complete remissions after CAR therapy are possible, a substantial proportion of patients relapse due to lack of CAR persistence^{6,7}, suggesting that understanding cellular mechanisms

of human memory CAR formation are crucial for improving CAR therapy outcomes.

LIPSTIC identifies ACD in CARs

Target recognition by CARs is major histocompatibility complex- and therefore CD8 coreceptor-independent¹⁴. We reasoned that target-induced labelling of CAR molecules within the immunologic synapse, instead of surface CD8 expression levels, could be used to distinguish and characterize first-division proximal- and distal-daughter CARs, as proximal-daughter CARs, by definition, have made physical contact with the target cell. We therefore optimized a technique known as labelling immune partnerships by sor-tagging intercellular contacts (LIPSTIC)¹⁵ to perform sortase A enzyme-mediated irreversible labelling of CAR molecules within the immunologic synapse (Fig. 1a and Extended Data Figs. 1 and 2a–e).

On formation of cell–cell conjugates, the LIPSTIC label is immediately enriched at the immune synapse and specifically transferred from the

¹Department of Dermatology, Perelman School of Medicine, University of Pennsylvania, Philadelphia, PA, USA. ²Center for Cellular Immunotherapies, Perelman School of Medicine, University of Pennsylvania, Philadelphia, PA, USA. ³Department of Pathology and Laboratory Medicine, Perelman School of Medicine, University of Pennsylvania, Philadelphia, PA, USA. ⁴Department of Biomedical Science, Hallym University, Chuncheon, Republic of Korea. ⁵Department of Dermatology, Vagelos College of Physicians and Surgeons, Columbia University, New York, NY, USA.

⁶These authors contributed equally: Casey S. Lee, Sisi Chen. ✉e-mail: asp2261@cumc.columbia.edu; chell@penncmedicine.upenn.edu

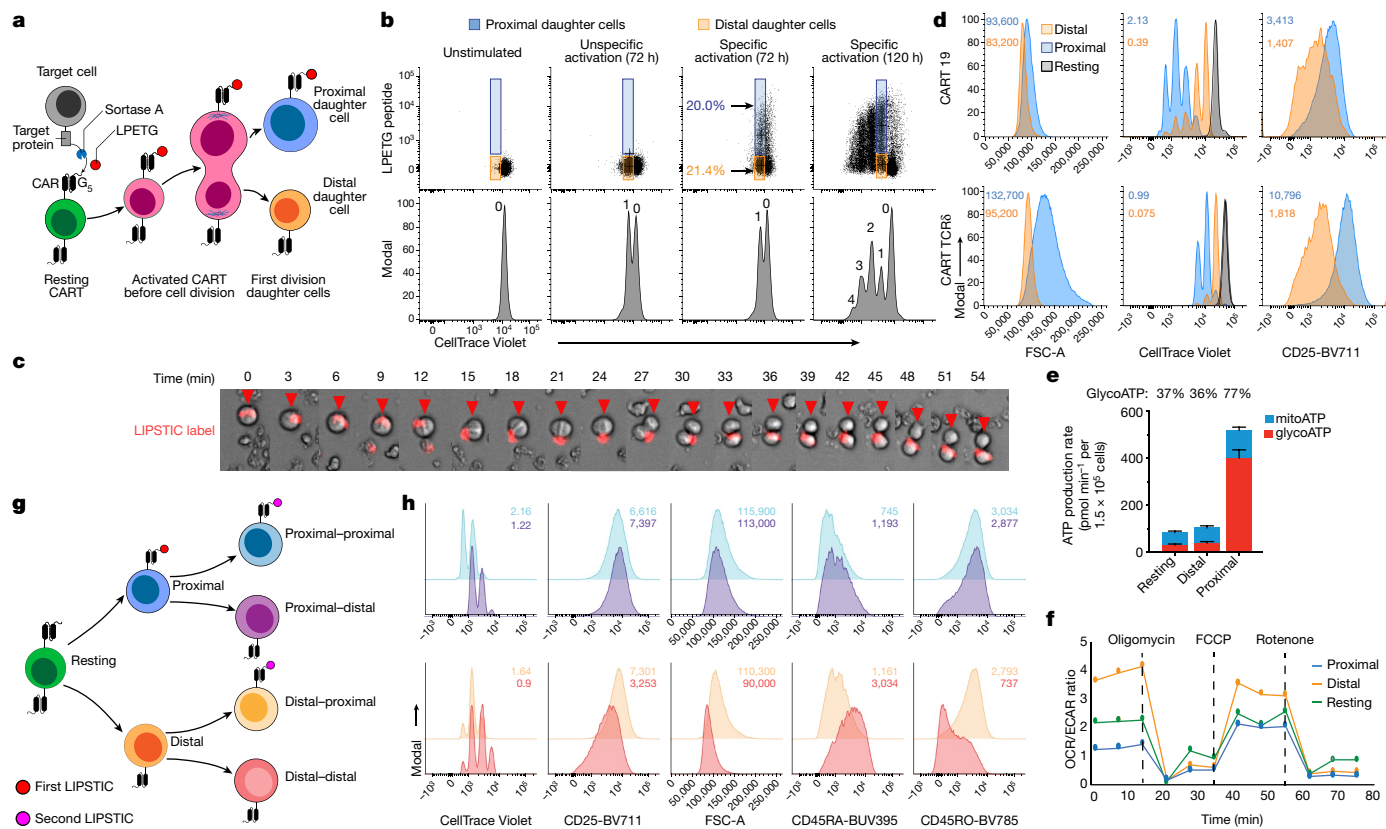


Fig. 1 | LIPSTIC distinguishes first-division proximal and distal-daughter CARTs. **a**, Schematic for the LIPSTIC assay to discriminate first-division proximal and distal-daughter CARTs. **b**, Representative flow cytometry plot of LIPSTIC labelling and cell division following activation. Unstimulated indicates donor-matched CARTs cultured without target cells. Unspecific activation indicates anti-CD3/anti-CD28 beads, versus specific activation through the CAR by LPETG-labelled target Nalm6 cells. Gating strategy in Extended Data Fig. 2g. **c**, LPETG label (red) retention on one daughter CART cell following first cell division after specific activation; photographs were acquired every 3 min. **d**, Representative flow cytometry histograms of bulk anti-CD19 and anti-TCR δ CARTs 3 days after isolating first-division daughter cells from in vitro coinoculation. **e**, ATP production rate of sorted first-division

proximal- and distal-daughter bulk CARTs comparing mitochondrial (mitoATP) to glycolytic (glycoATP) ATP production. Error bars indicate mean + standard deviation from four replicates for resting and distal and five replicates for proximal. **f**, Oxygen consumption rate (OCR)/extracellular acidification rate (ECAR) ratio of resting and sorted proximal- and distal-daughter CD8 CARTs. **g, h**, First-division distal-daughter CARTs show ACD following second target encounter. **g**, Schematic of isolating second-division daughter CARTs after second target engagement. **h**, Representative flow cytometry histograms of CD8 CART progeny 2 days after second-division daughter cell isolation. Median fluorescence intensity or division index is shown in the histogram plots (**d, h**). Plots are representative of 2–5 independent experiments with CARTs from distinct donors.

target to the CART cell (Supplementary Video 1 and Extended Data Fig. 2f). Flow cytometric characterization of first-division daughter CARTs demonstrates an equal percentage of LIPSTIC⁺ and LIPSTIC⁻ cells (Fig. 1b and Extended Data Fig. 2g), suggesting asymmetric distribution of LIPSTIC among first-division daughter cells. Live-cell imaging of LIPSTIC-labelled CART during the first mitosis after activation confirms that the LIPSTIC label is exclusively retained on one daughter cell during mitosis while the other daughter cell remains label-free (Fig. 1c and Supplementary Video 2).

LIPSTIC⁺ first-division daughter CARTs generated in vitro from bulk T cells show an increase in cell size, CD25 surface expression and subsequent proliferative pace (Fig. 1d and Extended Data Fig. 3a). Consistent with metabolic asymmetry observed in activated mouse T cells^{9,10}, LIPSTIC⁺ first-division daughter cells demonstrate increased metabolic activity compared to LIPSTIC⁻ first-division daughters and shift to glycolysis as their predominant metabolic state (Fig. 1e), supporting increased cell size and proliferation rate in proximal daughters. By contrast, distal daughters show only a minor increase in metabolic activity compared to resting T cells and rely predominantly on oxidative phosphorylation (Fig. 1f). Collectively, these data establish that the first cell division of human CARTs after activation is asymmetric and that LIPSTIC⁺ and LIPSTIC⁻ daughter cells represent proximal and distal-daughter CARTs, respectively.

ACD occurs across CART subsets

Most current FDA-approved CART therapies are heterogeneous infusion products manufactured from bulk T cells in various differentiation stages^{16–19}; nevertheless, we evaluated whether specific CART subsets (CD4/CD8, naive/effector) show ACD. First-division daughters of both CD8 and CD4 CARTs showed asymmetry in cell size, CD25 surface expression and subsequent proliferative pace across a range of CART:target ratios in vitro, findings that are mostly preserved after in vivo CART labelling (Extended Data Figs. 2a and 3b,c). To determine whether different immunophenotypic CART subsets show ACD, we generated CARTs from naive (CD62L⁺CD45RO⁻) or effector (CD62L⁻) T cells and phenotyped first-division daughter cells. First-division daughters of naive-derived CARTs showed asymmetry in cell size, CD25 expression and proliferative pace, similar to observations with bulk CARTs. First-division daughters of effector-derived CARTs showed a trend towards differences in proliferative pace, although minimal differences in CD25 and cell size were observed in effector-derived CARTs compared to naive-derived CARTs (Extended Data Fig. 3d,e).

To test whether ACD is restricted to the first cell division, we isolated first-division proximal- and distal-daughter CARTs and immediately re-exposed them to target cells bearing a different fluorescent LIPSTIC label (Fig. 1g and Extended Data Fig. 2a). We observed asymmetry in proliferation, cell size and surface expression of CD25, CD45RA and

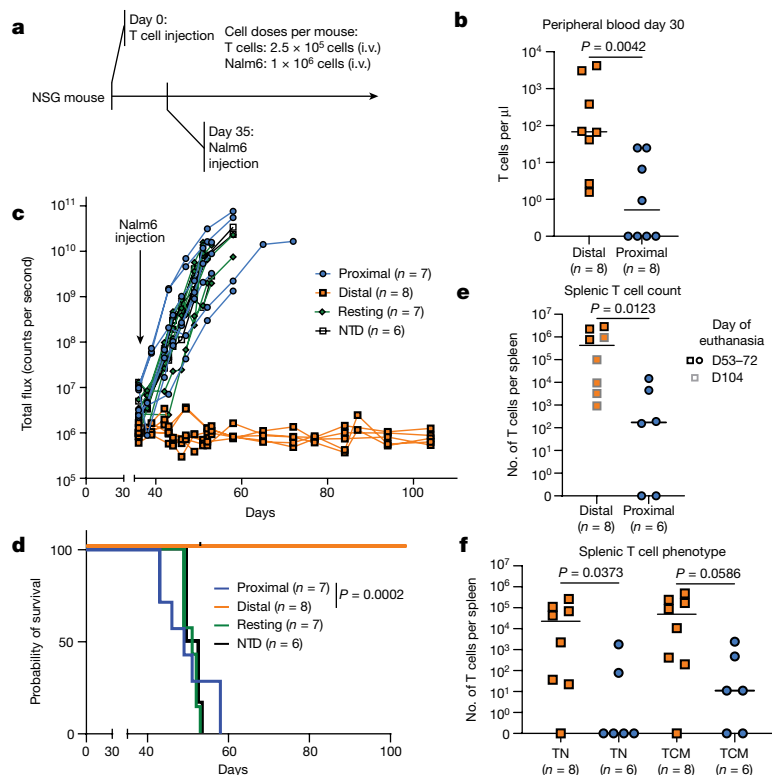


Fig. 2 | Distal-daughter CARTs show superior in vivo functional persistence. **a**, NSG mice are injected with proximal-daughter CARTs, distal-daughter CARTs, resting CARTs or non-transduced (NTD) T cells and subsequently challenged with Nalm6 cells 35 days later. **b**, Peripheral blood T cell count on 30 days after T cell injection. Lines represent the medians. **c**, Bioluminescence imaging quantification of Nalm6 cells in NSG mice. **d**, Kaplan–Meier survival curve.

Dashes indicate censored data. **e, f**, Splenic T cell counts. Lines represent the medians. **e**, Total splenic T cell counts. **f**, Splenic counts by T_{CM} (CD62L⁺CD45RA⁺) and T_N (CD62L⁺CD45RA⁻) phenotype. Data pooled from three independent experiments with distinct donors ($n = 6–8$ mice per condition). Statistical significance was determined using a log-rank test (**d**) and two-tailed Mann–Whitney test (**b, e, f**). i.v., intravenous.

CD45RO in progeny of second-division distal–proximal and distal–distal CARTs, whereas the phenotypes of proximal–proximal and proximal–distal CARTs paralleled those of effector CARTs, with a trend towards differences in proliferation rate but minimal differences in cell size and surface phenotypic markers (Fig. 1h and Extended Data Fig. 3f). Thus, CAR-induced ACD is widely detectable across T cell subsets and occurs both in vitro and in vivo, and distal-daughter cells retain the ability to undergo ACD on subsequent target cell encounter.

Longevity of distal-daughter CARTs

To test the functional relevance of the observed flow cytometric and metabolic asymmetry in first-division CARTs, we first compared the longevity of proximal daughters and distal daughters in vivo (Fig. 2a). We injected sorted proximal-daughter or distal-daughter CARTs into NOD. *Cg-Prkdc^{scid}Il2rg^{tm1Wjl}/SzJ* (NOD-scid-gamma (NSG)) mice, followed by injection of Nalm6 leukaemia cells 35 days later to evaluate engraftment and persistence of injected CARTs. Then 30 days after T cell injection, mice that received distal-daughter CARTs showed greater peripheral T cell counts compared to mice that received proximal-daughter CARTs, suggesting greater engraftment and persistence of distal-daughter CARTs in vivo (Fig. 2b). After Nalm6 challenge, only distal daughters were able to control leukaemic outgrowth (Fig. 2c,d and Extended Data Fig. 4a). Mice that received distal daughters had greater T cell counts in the spleen compared to mice that received proximal daughters and demonstrated a preservation of naive (T_N)-like immunophenotypes, suggesting continued in vivo self-renewal by distal-daughter CARTs (Fig. 2e,f). These data indicate that proximal daughters show short in vivo lifespan and functionally establish distal daughters as precursors of long-lived memory CART in vivo.

Effector function in distal daughter CARTs

We next characterized the cytotoxic capacity of first-division daughter cells in vitro. As expected, proximal daughters demonstrate potent cytotoxic activity with substantial killing at very low effector:target ratios, surpassing the cytotoxicity of resting CARTs (Fig. 3a). Unexpectedly, distal daughters also demonstrated potent cytotoxic activity, with similar specific lysis of target cells as proximal daughters at a 3:1 effector:target ratio (Fig. 3a). Distal daughters isolated from T_N -like or T_{eff} CARTs also showed similar cytotoxic potency to their proximal-daughter counterparts and were more cytolytic than their resting counterparts (Extended Data Fig. 4b,c), suggesting that the cytotoxic activity of distal daughters of bulk CARTs was not solely due to the enrichment of distal-daughter cells of a particular immunophenotypic subset. By day 4 after first cell division, however, the cytotoxic activity of distal daughters decreased and more closely resembled resting CARTs (Fig. 3a). These data indicate that target cell encounter and subsequent activation induces a transient state of increased cytotoxic potency in both proximal daughters and distal daughters, despite the latter showing an overall less activated flow cytometric and metabolic phenotype compared to proximal daughters and ultimately demonstrating greater ability for long-term in vivo persistence and function.

Next, we tested whether distal-daughter CARTs could show effector cytotoxic function in vivo (Fig. 3b). We used a previously established stress-test model in which subtherapeutic numbers of CARTs are injected into leukaemia-bearing mice to compare cytotoxic function and longevity between treatment groups^{20,21}. We observed an initial decline of leukaemia burden after treatment with proximal-daughter and distal-daughter CARTs, consistent with their cytotoxic activity in vitro (Fig. 3c and Extended Data Fig. 4d). However,

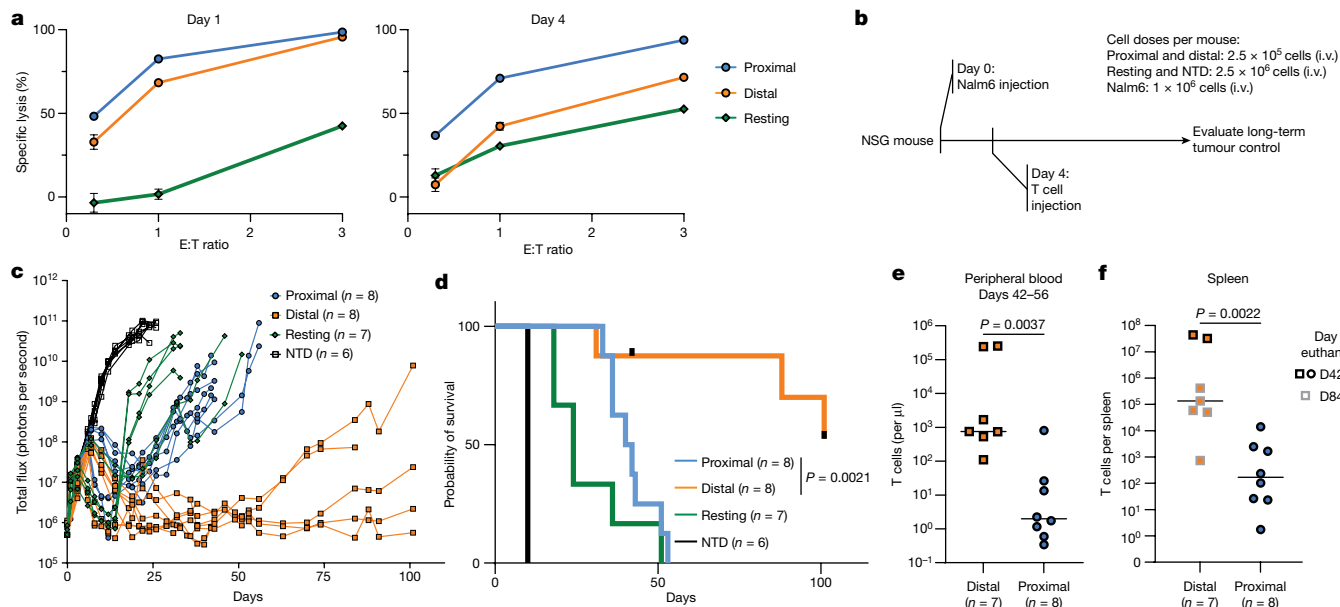


Fig. 3 | First-division daughter CARTs demonstrate distinct patterns of cytotoxic activity and in vivo leukaemia control. **a**, Twenty-hour in vitro cytotoxicity assay data performed 1 day (left) or 4 days (right) after first-division daughter cell isolation. Data points represent the mean of triplicates and error bars represent standard error of the mean. E:T, effector:target ratio. **b**, CARTs are injected into Nalm6-bearing NSG mice 4 days after engraftment. **c**, Bioluminescence imaging quantification of Nalm6 cells in NSG mice.

following the initial decline of leukaemia burden, mice treated with proximal-daughter CARTs had a gradual loss of leukaemia control consistent with a short-lived effector phenotype, whereas mice treated with distal daughters showed longer-term control of leukaemia outgrowth (Fig. 3d). Proximal-daughter CARTs showed reduced frequencies in blood on days 42–50, consistent with their terminal differentiation in vivo that resulted in reduced long-term leukaemia control, whereas distal-daughter CART progeny demonstrated long-term engraftment and greater splenic T cell counts up to day 101 (Fig. 3e,f). Thus, distal daughters transiently show effector functions in vivo and show greater longevity and replicative potential even with repeated target engagement. The therapeutic advantages of distal-daughter CARTs may be achieved without specifically isolating for distal daughters, because, despite receiving a lower T cell dose, mice treated with unsorted restimulated CARTs showed greater tumour control compared to mice treated with resting CARTs (Extended Data Fig. 4e–h). These findings highlight the potential benefit of on-target restimulation during CART manufacturing to achieve controlled, optimal CART expansion, which is a pivotal factor in CART therapy, especially as inadequate expansion is linked to poorer outcomes in malignancy control⁶.

Single-cell profiling of ACD in CD8 CARTs

Given the functional differences between proximal- and distal-daughter CARTs, we next sought to investigate the mechanisms during ACD that drive the distinct fates and functions of first-division daughter cells. We used single-cell profiling to simultaneously characterize CD8 CARTs in regard to surface protein expression, transcriptional activity and T cell receptor (TCR) clonality, an approach that better resolves subset identity of mature T cells compared to transcriptional analysis alone^{22,23} (Fig. 4a). Dimensionality reduction of antibody-derived sequencing data with uniform manifold approximation and projection (UMAP) demonstrates separation of resting from activated CARTs before the first cell division (Fig. 4b), reflecting activation-induced changes in the surface protein landscape of CD8 CARTs. First-division daughter cells

occupy the space between resting and activated-undivided T cells, with a clear distinction between proximal and distal daughters (Fig. 4b). These data indicate that activated CARTs establish asymmetry of the cell surface proteome during the first cell division.

d, Kaplan–Meier survival curve. Dashes indicate censored data. **e**, Peripheral blood T cell count on days 42–56 after Nalm6 injection. Lines represent the medians. **f**, Total splenic T cell counts. Lines represent the medians. Data pooled from three independent experiments with distinct donors ($n = 6–8$ mice per condition). Statistical significance was determined using a log-rank test in **d** and two-tailed Mann–Whitney test in **e,f**.

We performed unsupervised clustering of CD8 CARTs based on surface protein expression (Fig. 4c). Consistent with the asymmetric partitioning of surface proteins, clusters largely respect the borders between resting, distal and proximal daughters, and activated-undivided cells, allowing cluster-wise comparison of proximal and distal-daughter CARTs. An exception was cluster 6, which contained cells from both resting and distal-daughter populations but separated into two clusters consistent with distal-daughter and resting CARTs after increasing the clustering resolution (Extended Data Fig. 5a–c). We assigned clusters into four immunophenotypic subsets resembling T_N -like, central-memory (T_{CM})-like, effector-memory (T_{EM})-like and tissue-resident-memory (T_{RM})-like subsets based on a combination of surface protein expression and RNA expression (Fig. 4d and Extended Data Fig. 5d). Expanded T cell clones (defined by endogenous TCR α and TCR β chains) were highly enriched in T_{EM} and T_{RM} subsets (Extended Data Fig. 5e), consistent with clonal enrichment commonly found in effector subsets^{24,25}. Furthermore, 91% of expanded T cell clones were shared between proximal and distal CARTs, and proximal and distal CARTs demonstrate comparable TCR V-gene usage, thus demonstrating similar clonal distribution and independently supporting accurate identification of first-division proximal- and distal-daughter cells (Extended Data Fig. 5f,g).

Asymmetric division of surface proteome

We molecularly define the surface proteomic differences that distinguish proximal-daughter from distal-daughter CARTs. Pairwise comparison of proximal and distal daughters demonstrates increased surface expression for CD45RA on distal daughters and for CD25 on proximal daughters (Fig. 4e), consistent with our flow cytometry data. Distal daughters demonstrated a notable increase in CD5, which is of

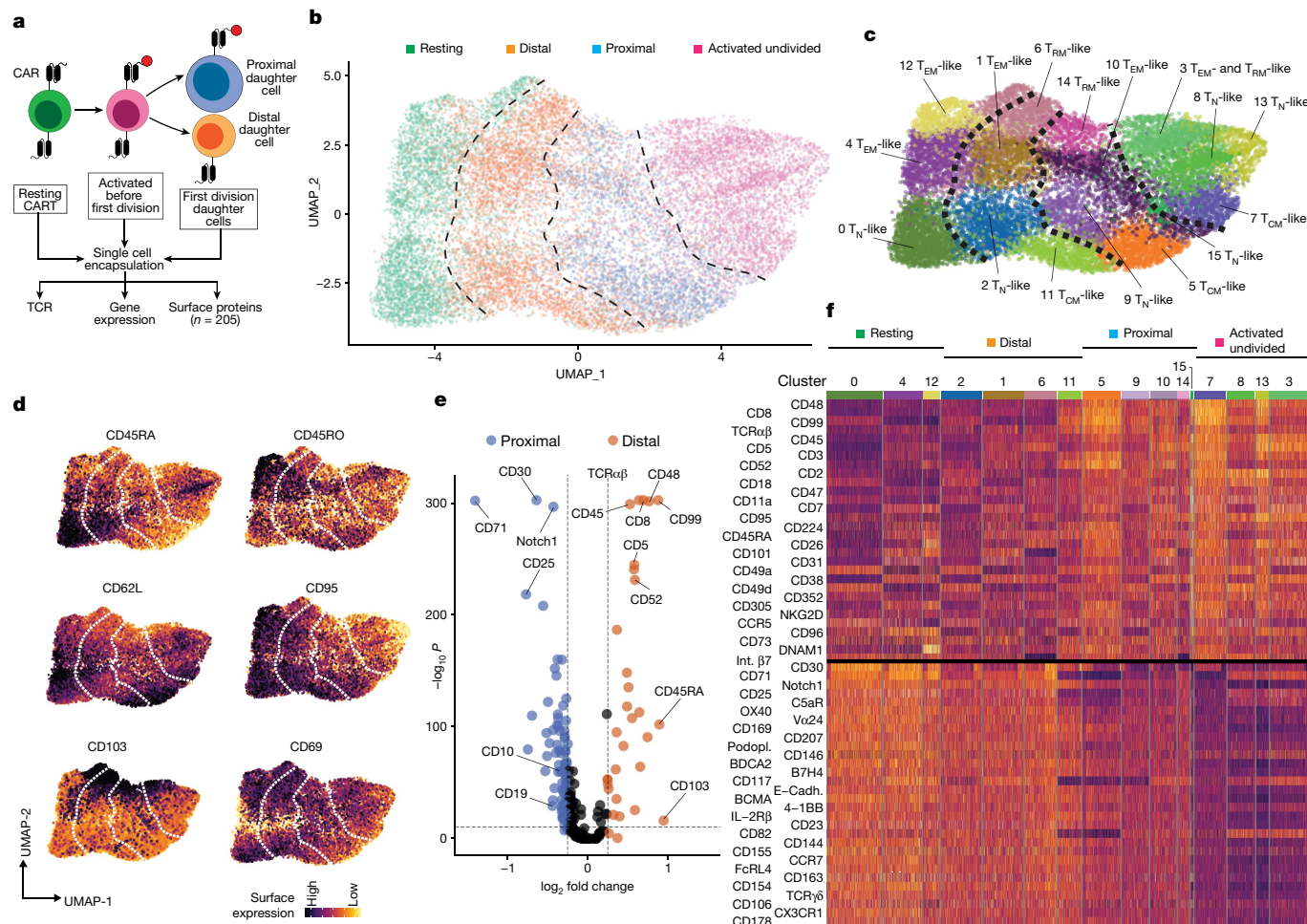


Fig. 4 | Proximal-daughter and distal-daughter CD8 CARTs show asymmetry in surface protein expression. **a**, Schematic for single-cell proteomic, transcriptomic and TCR analysis of first-division daughter, resting and activated CD8 CARTs before first cell division. **b, c**, UMAP plot using surface protein expression coloured by LIPSTIC assay cell population (**b**) and unsupervised clustering with cluster assignments made using a combination of transcriptional activity and surface proteins (**c**) as in Extended Data Fig. 5d. Dashed lines indicate borders between proximal, distal, resting and activated-undivided CARTs. **d**, Normalized single-cell surface protein levels. **e**, Volcano plot illustrating differentially abundant surface proteins on proximal-daughter and distal-

daughter CARTs. The dashed lines denote cut-offs defined by isotype controls (\log_2 fold change 0.25; adjusted P value 10^{-11}). **f**, Heat map of normalized surface protein levels showing the top 30 proteins enriched in either distal (top half) or proximal (bottom half) daughter CARTs in comparison to resting and activated-undivided CARTs. The top colour bar refers to clusters in **c**. Plots are representative of two independent experiments using the anti-CD19 CARTs and anti-TCR δ CARTs from distinct donors. Statistical significance was determined using two-tailed Wilcoxon rank-sum test with Benjamini-Hochberg correction for multiple comparisons (**e**).

interest given the previously reported antiproliferative effect of CD5 in human T cells²⁶. Proximal daughters showed enrichment of several proteins (for example, CD19 and CD10) expressed by B cells but not T cells. As CD19 and CD10 are expressed on Nalm6 cells and the CARTs do not show transcriptional activity for *CD19* and *CD10* (Extended Data Fig. 6a), we presume these proteins were transferred from target to CART by trogocytosis²⁷. In contrast to previous studies characterizing ACD in mouse or human T cells after stimulation of the endogenous TCR^{8,28}, we observed increased expression of the endogenous TCR and CD8 coreceptor on distal daughters as opposed to proximal daughters (Fig. 4e and Extended Data Fig. 6b). This phenomenon was independent of the CAR hinge as it occurred with both CD8- and IgG4-derived hinge domains (Extended Data Fig. 6c). Furthermore, we observe key phenotypes of ACD in the absence of endogenous TCR (Extended Data Fig. 6d-f). These findings highlight that CAR-induced ACD shows unique features compared to endogenous TCR-induced ACD.

distal daughters more closely resemble resting T cells (subset description in Extended Data Figs. 7-10). Overall, these data indicate that ACD affects the global surface proteome of activated CD8 CARTs, which may support the observed differential functional trajectories of proximal and distal CARTs following ACD.

CART transcriptomes diverge during ACD

As transcriptional programs drive CART function, we next characterized the single-cell transcriptome of CD8 CARTs. We observed predominant expression of *RUNX3* and *FLII* in effector cells with lower transcriptional activity in T_N- and T_{CM}-like cells (Fig. 5a and Extended Data Fig. 5d). When comparing within T_N-like, T_{CM}-like, T_{EM}-like and T_{RM}-like subsets, proximal and distal CARTs show global asymmetry in transcript abundances (Extended Data Figs. 7-10). Because previous studies have mainly characterized ACD in murine naive CD8 T cells, we initially focused on transcriptional differences between proximal and distal T_N-like clusters (Extended Data Fig. 7c). Consistent with these studies^{12,29}, T_N-like distal daughters expressed higher levels of *LEF1*, *TCF7*, *CCR7*, *IL7R* and *KLF2* compared to proximal daughters (Fig. 5b) and

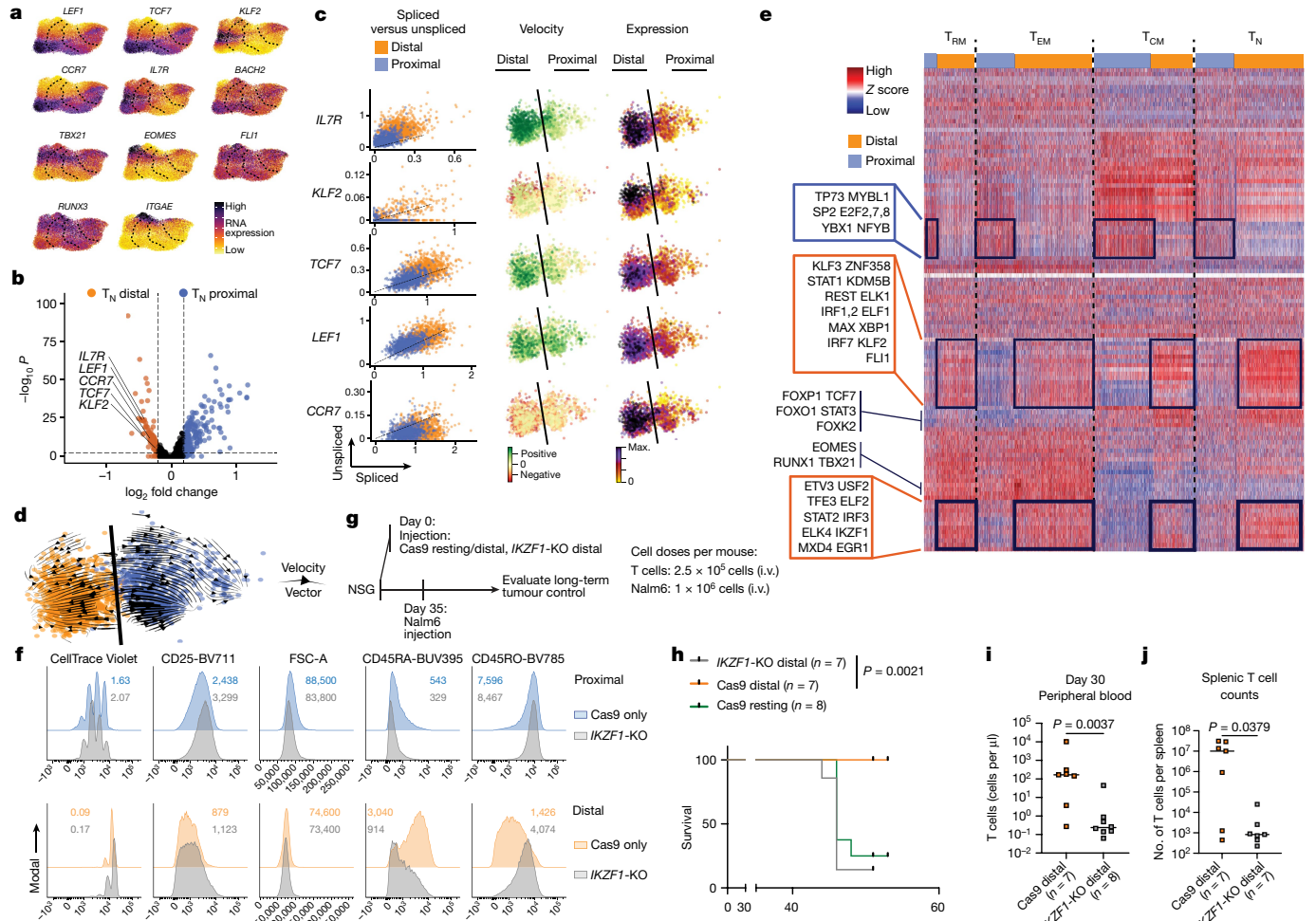


Fig. 5 | Proximal-daughter and distal-daughter CD8 CART fates are driven by divergent transcriptional programmes. **a**, Normalized single-cell gene expression levels. **b**, Volcano plot illustrating differentially expressed genes in CD8 T_N daughter CARTs. Dashed lines indicate cut-offs for log₂ fold change and -log₁₀P. **c**, Gene-specific RNA velocity shown as spliced or unspliced transcripts (left column) and projected onto T_N-like UMAP clusters from Extended Data Fig. 7c (middle column) in comparison to normalized gene expression levels (right column). **d**, Velocity vector projection onto T_N-like UMAP clusters. The black line signifies border between distal (orange) and proximal (blue) cells. **e**, Heat map of single-cell regulon activity of bulk CD8 CARTs; the top colour bar referencing proximal and distal cells separated by T cell subset assignment (from Extended Data Fig. 5). The blue box shows the shared transcription factor set with increased activity in proximal daughters; orange boxes show the shared transcription factor set with increased activity in distal daughters. **f**, Flow cytometry histogram plots of CD8 proximal-daughter (top) and

distal-daughter (bottom) *IKZF1*-knockout (KO) and wild-type CARTs. Median fluorescence intensity or division index is shown in the histogram plots. **g**, NSG mice are injected with *IKZF1*-KO distal, wild-type distal and wild-type resting CARTs and subsequently challenged with Nalm6 cells 35 days later. **h**, Kaplan-Meier survival curve. Dashes represent censored data. **i**, Peripheral blood T cell count on 30 days after T cell injection. Lines represent the medians. **j**, Total splenic T cell count. Lines represent the medians. **a-f** Representative of two independent experiments using the anti-CD19 CARTs and anti-TCR8 CARTs from distinct donors. **f**, Representative of three independent experiments with summary plots in Extended Data Fig. 11d. **h-j**, Data pooled from two experiments with distinct donors ($n = 7-8$ mice per condition). Statistical significance was determined using a two-tailed Wilcoxon rank-sum test with Benjamini-Hochberg correction for multiple comparisons (**b**), log-rank test (**h**) and two-tailed Mann-Whitney test (**i, j**).

gene-set enrichment analysis indicates enrichment of naive signatures and repression of effector-associated genes in distal-daughter CARTs, indicating an asymmetric abundance of transcripts characteristic of naive and memory precursors in first-division T_N-like daughter cells (Extended Data Fig. 7d). Consistent with previous reports on metabolic asymmetry among first-division daughter cells for factors downstream of *MYC*^{9,10,13}, proximal daughters are enriched for *MYC* and *MTORC1* target genes and show a glycolytic gene signature (Extended Data Fig. 7d,e).

We addressed whether the transcriptional asymmetry was a result of uneven partitioning of pre-existing RNA or due to transcriptional up- or downregulation of fate-regulating genes after ACD. Using RNA velocity analysis^{30,31}, we quantified the ratio of unspliced to spliced transcripts to detect short-term changes in gene expression state in first-division

daughter CARTs (Fig. 5c). In addition to increased transcript abundance, we observed increased positive velocity of *IL7R*, *KLF2*, *TCF7* and *LEF1* expression in distal daughters compared to proximal daughters, indicating transcriptional upregulation of these genes following the first cell division. There was a notable absence of unspliced *KLF2* transcripts in proximal daughters, indicating marked downregulation of transcriptional activity. Although the *CCR7* transcript abundance was higher in distal daughters, *CCR7* RNA velocity was similarly neutral or negative in both proximal daughters and distal daughters, suggesting that the difference in *CCR7* transcripts is a result of uneven RNA distribution during the first cell division rather than asymmetric changes in transcription. These results underscore that both asymmetric partitioning of pre-existing RNA and changes in transcriptional activity are mechanisms driving transcript-level differences during ACD.

To visualize cell-state trajectories, we projected single-cell RNA velocity vectors onto the surface protein-based proximal and distal UMAP T_N -like clusters, extrapolating similar states to other cells in local proximity (Fig. 5d). Although proximal daughters and distal daughters each demonstrate similar internal trajectories, the trajectory direction of proximal daughters compared to distal daughters is diametrically opposed, indicating that proximal and distal daughters activate distinct transcriptional programmes that support their divergent differentiation and cell-state trajectories. We observed similar opposed trajectories in T_{CM} , T_{EM} and T_{RM} -like clusters (Extended Data Figs. 8–10). Thus, proximal- and distal-daughter cells show distinct transcriptional programmes and trajectories, driven by both asymmetric RNA partitioning and postdivision gene regulation.

Transcription factor core sets in daughter CARTs after ACD

To explain regulatory networks driving the observed transcriptional changes after ACD, we used single-cell regulatory network inference and clustering (pySCENIC³²) to compare the activities of transcription factor-associated gene networks, or regulons, across all (T_N , T_{CM} , T_{EM} and T_{RM} -like) CD8 CART subsets and between proximal daughters and distal daughters (Fig. 5e). Regulon activity supported our previous subset assignment, as T_N - and T_{CM} -like cells demonstrated increased *TCF7*, *FOXP1*, *STAT3* regulon activity, contrasting with T_{EM} - and T_{RM} -like cells, which demonstrated increased activity of *EOMES*, *TBX21* and *RUNX1* regulons.

When comparing regulon activities between all proximal daughters and distal daughters, we observed that proximal daughters upregulated regulons associated with apoptosis, proliferation and effector cell differentiation (Fig. 5e, blue box), including *TP73*, a member of the pro-apoptotic p53 superfamily and known to be highly expressed in short-lived plasmablasts³³; proproliferative *E2F* family members 2, 7 and 8 (ref. 34); *MYBL1*, a repressor of naive and memory T cell function³⁵ and *YBX1*, which is associated with early effector differentiation¹².

By contrast, we identified within all distal-daughter cells increased regulon activity across a group of transcription factors that have previously been associated with an antiproliferative and self-renewing transcriptional program (Fig. 5e, orange boxes). This shared transcription factor profile of distal-daughter CARTs includes *KLF2*, a repressor of chemokine receptor expression³⁶ and activator of CD62L and S1PR1 expression³⁷; *IRF1*, whose loss results in increased proliferation and reduced protection in the context of viral infection³⁸; and other transcription factors associated with interferon stimulation (*IRF2*, *IRF3*, *IRF7*, *IRF9* and *STAT2*). The shared set also encompasses *STAT1*, which is important for quiescence³⁹ and self-renewal⁴⁰ of CD8 T cells and inhibits proliferation⁴¹; *KDMSB*, a histone deacetylase upregulated in T_{RM} precursors early after viral infections⁴²; *REST*, a transcriptional repressor upregulated in quiescent human T cells⁴³ and after PD-1 blockade⁴⁴; *FLII*, which is critical for limiting effector T cell expansion⁴⁵; *MXD4*, a negative regulator of *MYC* that promotes T cell survival and memory formation^{46,47} and *IKZF1*, a transcription factor that inhibits expression of *IL2* and *IL2RA* (CD25) and restrains CD8 effector differentiation^{48,49}.

To test the functional relevance of the core transcription factor in ACD and its effect on the fate of distal-daughter CARTs, we used CRISPR–Cas9 technology to create a permanent knockout of *IKZF1*, which has not been implicated in the context of ACD and was chosen due to its role in restraining T cell proliferation, sensitivity to activation and effector differentiation^{49–52}. The absence of *IKZF1* resulted in distal-daughter cells that showed a phenotype similar to that of proximal daughters, marked by a loss of CD45RA, signifying a shift towards increased effector differentiation (Fig. 5f and Extended Data Fig. 11a–d). As a complementary approach, we transiently depleted *IKZF1* using the therapeutic agent lenalidomide⁵³, which was administered just before CART exposure to target cells (Extended Data Fig. 11e,f). Similar to the

knockout, this transient depletion resulted in distal daughters losing CD45RA and gaining CD25 expression, further supporting the role of *IKZF1* in contributing to the immunophenotype of distal daughters during ACD (Extended Data Fig. 11g). We then evaluated the importance of *IKZF1* for the persistence and long-term function of distal-daughter CARTs in vivo. *IKZF1*-knockout distal daughters showed reduced T cell count in the circulation 30 days after injection in NSG mice, diminished control of Nalm6 tumour and lower T cell counts in the spleen (Fig. 5g–j and Extended Data Fig. 11h). These observations highlight that, independent of traditional naive, memory or effector T cell surface markers expressed at the time of cell isolation, proximal-daughter versus distal-daughter cell identity initiated by ACD induces distinct sets of transcriptional programs that can confer different functions and fates in T cell progeny, with *IKZF1* serving as an essential transcription factor for distal-daughter cell cytotoxic function and persistence in vivo.

Discussion

Taken together, our work establishes that human CD8 CARTs use ACD to induce differential cell fates after target encounter and that first-division proximal- and distal-daughter cells constitute distinct cellular subtypes. Through target-induced proximity labelling of CAR molecules on proximal-daughter CARTs, we distinguish and isolate proximal-daughter and distal-daughter CARTs and perform unbiased single-cell profiling of their surface proteome and transcriptional program, combined with functional analyses of subsequent cell division asymmetry, cytotoxic potency and in vivo longevity. Beyond previous reports that identified asymmetric sorting of specific molecules in non-engineered human or murine T cells^{8–10,13,28,29,54–56}, we find that the global surface proteome undergoes asymmetric sorting during the first cell division. CARTs demonstrate a unique pattern of protein asymmetry, with a notable enrichment of endogenous TCR complex proteins (TCR $\alpha\beta$, CD3 and CD8) on distal daughters, an unexpected finding that may have hindered previous discovery of ACD in human CARTs¹⁴. Our data mechanistically link differential fate trajectories to both cell-intrinsic transcriptional regulation after ACD and asymmetric partitioning of RNA during ACD. Specifically, upregulation of *IL7R* expression, whose gene product (CD127) is widely recognized as a marker of memory precursors^{12,57}, occurs within hours of the first cell division in distal-daughter CARTs, as evidenced by increased RNA velocity. Conversely, *CCR7* transcripts undergo asymmetric partitioning without detectable change in velocity. Unbiased transcriptome-wide trajectory analysis thus establishes a framework that contrasts with the traditional model of selecting cells based on a snapshot of cell surface marker or transcription factor expression, which at the time of detection may be up- or downregulating and could lead to progeny with heterogeneous fates.

Our work establishes that first-division daughter cells show unique transcriptional and functional attributes that set them apart from previously described CART subsets. Despite transcriptional heterogeneity of first-division daughter cells¹², shared sets of transcription factors known to promote or restrain proliferation and differentiation in T cells are active in first-division daughter CARTs regardless of traditional naive, memory or effector surface markers expressed at the time of CART isolation. The contrasting core transcriptional programs of proximal-daughter and distal-daughter CARTs establish ACD as a means of divergent fate induction beyond previous published studies on naive murine T cells, and modulating members of these core transcriptional programs such as *IKZF1* can alter the memory and effector balance of CART progeny. Furthermore, our data indicate that distal-daughter CARTs, in addition to demonstrating a memory-precursor transcriptome, aerobic metabolism and in vivo longevity, pass through a transient state of potent effector function that allows them to rapidly clear malignant cells. These unique features make distal-daughter CARTs and their transcriptional programs attractive for therapeutic applications.

ACD may not be the only mechanism of CART differentiation, but our findings may help to address past debate on whether memory T cells develop from effector or naive T cells. Whereas distal-daughter CARTs become destined to differentiate into long-lived memory cells by means of ACD, they also transiently show effector-like behaviour, and this cytotoxic plasticity in the days following ACD may reconcile observations of both naive⁹ and effector cells⁵⁸ as possible memory precursors.


In conclusion, our studies identify ACD as a mechanism for the generation of human memory CARTs along with transcriptional, surface proteomic and metabolic profiles of memory and effector precursors. Given the importance of memory CARTs for clinical outcomes, our studies provide an actionable framework that may be broadly applicable for optimization of CART and other T cell immunotherapies.

Online content

Any methods, additional references, Nature Portfolio reporting summaries, source data, extended data, supplementary information, acknowledgements, peer review information; details of author contributions and competing interests; and statements of data and code availability are available at <https://doi.org/10.1038/s41586-024-07862-7>.

- Park, J. H. et al. Long-term follow-up of CD19 CAR therapy in acute lymphoblastic leukemia. *N. Engl. J. Med.* **378**, 449–459 (2018).
- Maude, S. L. et al. Chimeric antigen receptor T cells for sustained remissions in leukemia. *N. Engl. J. Med.* **371**, 1507–1517 (2014).
- Melenhorst, J. J. et al. Decade-long leukaemia remissions with persistence of CD4⁺ CAR T cells. *Nature* **602**, 503–509 (2022).
- Porter, D. L. et al. Chimeric antigen receptor T cells persist and induce sustained remissions in relapsed refractory chronic lymphocytic leukemia. *Sci. Transl. Med.* **7**, 303ra139–303ra139 (2015).
- Brentjens, R. J. et al. CD19-targeted T cells rapidly induce molecular remissions in adults with chemotherapy-refractory acute lymphoblastic leukemia. *Sci. Transl. Med.* **5**, 177ra138–177ra138 (2013).
- Hay, K. A. et al. Factors associated with durable EFS in adult B-cell ALL patients achieving MRD-negative CR after CD19 CAR T-cell therapy. *Blood* **133**, 1652–1663 (2019).
- Fraietta, J. A. et al. Determinants of response and resistance to CD19 chimeric antigen receptor (CAR) T cell therapy of chronic lymphocytic leukemia. *Nat. Med.* **24**, 563–571 (2018).
- Chang, J. T. et al. Asymmetric T lymphocyte division in the initiation of adaptive immune responses. *Science* **315**, 1687–1691 (2007).
- Verbist, K. C. et al. Metabolic maintenance of cell asymmetry following division in activated T lymphocytes. *Nature* **532**, 389–393 (2016).
- Pollizzi, K. N. et al. Asymmetric inheritance of mTORC1 kinase activity during division dictates CD8⁽⁺⁾ T cell differentiation. *Nat. Immunol.* **17**, 704–711 (2016).
- Ciocca, M. L., Barnett, B. E., Burkhardt, J. K., Chang, J. T. & Reiner, S. L. Cutting edge: asymmetric memory T cell division in response to rechallenge. *J. Immunol.* **188**, 4145–4148 (2012).
- Kakaradov, B. et al. Early transcriptional and epigenetic regulation of CD8⁽⁺⁾ T cell differentiation revealed by single-cell RNA sequencing. *Nat. Immunol.* **18**, 422–432 (2017).
- Guo, A. et al. cBAF complex components and MYC cooperate early in CD8⁺ T cell fate. *Nature* <https://doi.org/10.1038/s41586-022-04849-0> (2022).
- Dotti, G., Gottschalk, S., Savoldo, B. & Brenner, M. K. Design and development of therapies using chimeric antigen receptor-expressing T cells. *Immunol. Rev.* **257**, 107–126 (2014).
- Pasqual, G. et al. Monitoring T cell-dendritic cell interactions in vivo by intercellular enzymatic labelling. *Nature* **553**, 496–500 (2018).
- Ghassemi, S. et al. Reducing ex vivo culture improves the antileukemic activity of chimeric antigen receptor (CAR) T cells. *Cancer Immunol. Res.* **6**, 1100–1109 (2018).
- Rafiq, S., Hackett, C. S. & Brentjens, R. J. Engineering strategies to overcome the current roadblocks in CAR T cell therapy. *Nat. Rev. Clin. Oncol.* **17**, 147–167 (2020).
- Sheih, A. et al. Clonal kinetics and single-cell transcriptional profiling of CAR-T cells in patients undergoing CD19 CAR-T immunotherapy. *Nat. Commun.* **11**, 219 (2020).
- Sommermeier, D. et al. Chimeric antigen receptor-modified T cells derived from defined CD8⁺ and CD4⁺ subsets confer superior antitumor reactivity in vivo. *Leukemia* **30**, 492–500 (2016).
- Zhao, Z. et al. Structural design of engineered costimulation determines tumor rejection kinetics and persistence of CAR T cells. *Cancer Cell* **28**, 415–428 (2015).
- Brentjens, R. J. et al. Eradication of systemic B-cell tumors by genetically targeted human T lymphocytes co-stimulated by CD80 and interleukin-15. *Nat. Med.* **9**, 279–286 (2003).
- Hao, Y. et al. Integrated analysis of multimodal single-cell data. *Cell* **184**, 3573–3587. e3529 (2021).
- Stuart, T. et al. Comprehensive integration of single-cell data. *Cell* **177**, 1888–1902.e1821 (2019).
- Wensveen, F. M. et al. Apoptosis threshold set by Noxa and Mcl-1 after T cell activation regulates competitive selection of high-affinity clones. *Immunity* **32**, 754–765 (2010).
- Qi, Q. et al. Diversity and clonal selection in the human T-cell repertoire. *Proc. Natl Acad. Sci. USA* **111**, 13139–13144 (2014).
- Shifrut, E. et al. Genome-wide CRISPR screens in primary human T cells reveal key regulators of immune function. *Cell* **175**, 1958–1971.e1915 (2018).
- Hamieh, M. et al. CAR T cell trogocytosis and cooperative killing regulate tumour antigen escape. *Nature* **568**, 112–116 (2019).
- Borsa, M. et al. Modulation of asymmetric cell division as a mechanism to boost CD8⁽⁺⁾ T cell memory. *Sci. Immunol.* **4**, eaav1730 (2019).
- Arsenio, J. et al. Early specification of CD8⁺ T lymphocyte fates during adaptive immunity revealed by single-cell gene-expression analyses. *Nat. Immunol.* **15**, 365–372 (2014).
- Bergen, V., Lange, M., Peidli, S., Wolf, F. A. & Theis, F. J. Generalizing RNA velocity to transient cell states through dynamical modeling. *Nat. Biotechnol.* **38**, 1408–1414 (2020).
- La Manno, G. et al. RNA velocity of single cells. *Nature* **560**, 494–498 (2018).
- Van de Sande, B. et al. A scalable SCENIC workflow for single-cell gene regulatory network analysis. *Nat. Protoc.* **15**, 2247–2276 (2020).
- Monaco, G. et al. RNA-seq signatures normalized by mRNA abundance allow absolute deconvolution of human immune cell types. *Cell Rep.* **26**, 1627–1640.e1627 (2019).
- Attwooll, C., Lazzarini Denchi, E. & Helin, K. The E2F family: specific functions and overlapping interests. *EMBO J.* **23**, 4709–4716 (2004).
- Best, J. A. et al. Transcriptional insights into the CD8⁺ T cell response to infection and memory T cell formation. *Nat. Immunol.* **14**, 404–412 (2013).
- Sebzda, E., Zou, Z., Lee, J. S., Wang, T. & Kahn, M. L. Transcription factor KLF2 regulates the migration of naive T cells by restricting chemokine receptor expression patterns. *Nat. Immunol.* **9**, 292–300 (2008).
- Carlson, C. M. et al. Kruppel-like factor 2 regulates thymocyte and T-cell migration. *Nature* **442**, 299–302 (2006).
- Brien, J. D. et al. Interferon regulatory factor-1 (IRF-1) shapes both innate and CD8⁺ T cell immune responses against West Nile virus infection. *PLoS Pathog.* **7**, e1002230 (2011).
- Kye, Y.-C. et al. STAT1 maintains naive CD8⁺ T cell quiescence by suppressing the type I IFN-STAT4-mTORC1 signaling axis. *Sci. Adv.* **7**, eabg8764 (2021).
- Huang, Z. et al. IL-27 promotes the expansion of self-renewing CD8⁺ T cells in persistent viral infection. *J. Exp. Med.* **216**, 1791–1808 (2019).
- Gil, M. P., Salomon, R., Louten, J. & Biron, C. A. Modulation of STAT1 protein levels: a mechanism shaping CD8 T-cell responses in vivo. *Blood* **107**, 987–993 (2006).
- Kurd, N. S. et al. Early precursors and molecular determinants of tissue-resident memory CD8⁽⁺⁾ T lymphocytes revealed by single-cell RNA sequencing. *Sci. Immunol.* **5**, eaaz6894 (2020).
- Zhang, W. et al. Genomic expression analysis by single-cell mRNA differential display of quiescent CD8 T cells from tumour-infiltrating lymphocytes obtained from in vivo liver tumours. *Immunology* **127**, 83–90 (2009).
- Pauken, K. E. et al. Epigenetic stability of exhausted T cells limits durability of reinvigoration by PD-1 blockade. *Science* **354**, 1160–1165 (2016).
- Chen, Z. et al. In vivo CD8⁽⁺⁾ T cell CRISPR screening reveals control by Flt1 in infection and cancer. *Cell* **184**, 1262–1280.e1222 (2021).
- Vasilevsky, N. A., Ruby, C. E., Hurlin, P. J. & Weinberg, A. D. OX40 engagement stabilizes Mxd4 and Mnt protein levels in antigen-stimulated T cells leading to an increase in cell survival. *Eur. J. Immunol.* **41**, 1024–1034 (2011).
- Heckler, M. et al. Inhibition of CDK4/6 promotes CD8 T-cell memory formation. *Cancer Discov.* **11**, 2564–2581 (2021).
- Clambey, E. T. et al. The Ikaros transcription factor regulates responsiveness to IL-12 and expression of IL-2 receptor alpha in mature, activated CD8 T cells. *PLoS ONE* **8**, e57435 (2013).
- O'Brien, S. et al. Ikaros imposes a barrier to CD8⁺ T cell differentiation by restricting autorecrite IL-2 production. *J. Immunol.* **92**, 5118–5129 (2014).
- Karginov, T. A., Ménot, A. & Vella, A. T. Optimal CD8⁺ T cell effector function requires costimulation-induced RNA-binding proteins that reprogram the transcript isoform landscape. *Nat. Commun.* **13**, 3540 (2022).
- Avitahl, N. et al. Ikaros sets thresholds for T cell activation and regulates chromosome propagation. *Immunity* **10**, 333–343 (1999).
- Winandy, S., Wu, P. & Georgopoulos, K. A dominant mutation in the Ikaros gene leads to rapid development of leukemia and lymphoma. *Cell* **83**, 289–299 (1995).
- Krönke, J. et al. Lenalidomide causes selective degradation of IKZF1 and IKZF3 in multiple myeloma cells. *Science* **343**, 301–305 (2014).
- Liedmann, S. et al. Localization of a TORC1-eIF4F translation complex during CD8⁺ T cell activation drives divergent cell fate. *Mol. Cell* **82**, 2401–2414.e2409 (2022).
- Ahmed, R., Bevan, M. J., Reiner, S. L. & Fearon, D. T. The precursors of memory: models and controversies. *Nat. Rev. Immunol.* **9**, 662–668 (2009).
- Kakaradov, B. et al. Early transcriptional and epigenetic regulation of CD8⁺ T cell differentiation revealed by single-cell RNA sequencing. *Nat. Immunol.* **18**, 422–432 (2017).
- Joshi, N. S. et al. Inflammation directs memory precursor and short-lived effector CD8⁺ T cell fates via the graded expression of T-bet transcription factor. *Immunity* **27**, 281–295 (2007).
- Youngblood, B. et al. Effector CD8 T cells dedifferentiate into long-lived memory cells. *Nature* **552**, 404–409 (2017).

Publisher's note Springer Nature remains neutral with regard to jurisdictional claims in published maps and institutional affiliations.

 **Open Access** This article is licensed under a Creative Commons Attribution-NonCommercial-NoDerivatives 4.0 International License, which permits any non-commercial use, sharing, distribution and reproduction in any medium or format, as long as you give appropriate credit to the original author(s) and the source, provide a link to the Creative Commons licence, and indicate if you modified the licensed material. You do not have permission under this licence to share adapted material derived from this article or parts of it. The images or other third party material in this article are included in the article's Creative Commons licence, unless indicated otherwise in a credit line to the material. If material is not included in the article's Creative Commons licence and your intended use is not permitted by statutory regulation or exceeds the permitted use, you will need to obtain permission directly from the copyright holder. To view a copy of this licence, visit <http://creativecommons.org/licenses/by-nc-nd/4.0/>.

© The Author(s) 2024

Methods

Lentiviral constructs and production, in vitro transcription, cell lines and cell culture

All cells in this study were cultured in RPMI 1640 supplemented with 10% fetal bovine serum (FBS), 10 mM HEPES and 1% penicillin/streptomycin at 37 °C in fully humidified environment with 5% CO₂ unless otherwise indicated. Cell lines were evaluated for mycoplasma contamination.

We used single chain variable fragment (scFv)-based CARs against human CD19 (clone FMC63) and the human TCR δ chain (clone 5A6.E9) with an appended N-terminal pentaglycine tag in a third generation lentiviral backbone (Extended Data Fig. 1). Both CAR constructs used scFVs in the light-chain-heavy-chain configuration followed by a CD8 α hinge and transmembrane domain and CD137 and CD3 ζ cytoplasmic domains. Furthermore, CARs were cloned with an IgG4 hinge instead of CD8 α hinge domains (Extended Data Fig. 6c) with standard cloning methods.

To create a human CD19-sortase construct, we cloned human CD19 (C-terminal truncation) into a third generation lentiviral backbone that provided an IgH signal peptide followed by a flag-tag, low-affinity sortase mutant¹⁵ and a linker peptide. Similarly, we cloned a $\gamma\delta$ TCR (clone PEER⁵⁹) into this vector (both chains as a single transcript separated by a P2A site). Constructs were obtained as double-stranded DNA (dsDNA) fragments from IDT, digested and ligated into the lentiviral backbones using standard cloning techniques. We cloned extra TCR chains into lentiviral backbones (CD3 γ -P2A-CD3 δ and CD3 ζ -P2A-CD3 ϵ plasmids) to facilitate expression of the $\gamma\delta$ TCR in non-T cell lines. Nucleotide and amino acid sequences of all constructs used in this study are listed in Supplementary Table 1. Lentivirus was produced as previously described using Lenti-X 293T cells^{60,61}.

For in vitro messenger RNA (mRNA) transcription, CAR constructs were cloned into a pDrive.150 poly(A) backbone⁶² using standard cloning techniques and linear mRNA was transcribed using the T7 mScript Standard mRNA Production System (Cellscript). Linear dsDNA templates were generated by digesting with either ClaI or SpeI, and mRNA was synthesized following the manufacturer's recommendations for a Cap 1-mRNA and roughly 150 base-long poly(A)-tail. mRNA was purified with an RNeasy Mini Kit (Qiagen), eluted in RNase-free water at 1 $\mu\text{g } \mu\text{l}^{-1}$ and aliquoted and stored at -80 °C.

To disrupt the endogenous CD19 locus in Nalm6 cells (provided by M. Milone, originally obtained from DSMZ) and to create a cell line only expressing CD19-sortase or $\gamma\delta$ TCR-sortase, two guide RNAs targeting the human CD19 locus were obtained (IDT, sequences in Supplementary Table 2) and 5 $\times 10^6$ Nalm6 cells were electroporated with a total of 50 pM ribonucleoprotein (consisting of Cas9 (IDT) and single-guide RNA (sgRNA)) in a total volume of 20 μl of Lonza P3 buffer (P3 primary cell 4D-Nucleofector X kit S) with a Lonza 4D-Nucleofector Core Unit (pulse protocol EO115) according to the manufacturer's protocol. After CD19 disruption, Nalm6 cells were cultured at 0.2–1 $\times 10^6$ cells per ml in standard medium for 14 days before sorting CD19 negative cells by FACS (BD Biosciences AriaII). Initial disruption efficiency was greater than 90%, which increased to more than 99% after sorting. CD19 negative Nalm6 cells were transduced with target proteins (CD3 γ , CD3 δ , CD3 ζ , CD3 ϵ , $\gamma\delta$ TCR-sortase or CD19-sortase) and positive cells were enriched by FACS.

All target cells in this study express green fluorescent protein (GFP)-click beetle green luciferase. Target cells were sorted on a regular basis to ensure persistence of the luciferase and surface antigen expression over several passages.

Bulk and CD8 CART production

Bulk or CD8 only primary human T cells from healthy donors were obtained from the University of Pennsylvania Human Immunology Core, stimulated with anti-CD3/anti-CD28 beads (Dynabeads, Thermo Fisher) for 24 h before transduction with lentiviral CAR constructs.

Anti-CD3/anti-CD28 magnetic beads were removed on day 4 after transduction and the IL-2 concentration was gradually lowered from 100 to 25 IU ml⁻¹ by day 8 after activation and 0 IU ml⁻¹ by day 10 after activation. Cell medium replacement and quantification of cell size and number (Coulter Multisizer 4e) occurred every 2–3 days. CAR transduction efficiency was determined by flow using a polyclonal antimurine Fab antibody conjugated to biotin (Jackson ImmunoResearch) and streptavidin-PE. Non-transduced T cells from the same donor were stained under identical conditions and used as negative control.

To generate naive or effector CARTs, naive and effector T cells were isolated from bulk primary human T cells and were electroporated with mRNA encoding CARs. Naive T cells were isolated either with the Naive Pan T Cell Isolation Kit (Miltenyi Biotec, catalogue no. 130-097-095) or with a positive selection of CD62L and subsequent negative selection for CD45RA⁺ cells. For the latter approach, cells were stained with anti-CD62L-PE (BioLegend, DREG-56, catalogue no. 304840) and enriched with the anti-PE MultiSort kit (Miltenyi Biotec, catalogue no. 130-090-757) and LS column (Miltenyi Biotec, catalogue no. 130-042-401), with the flowthrough reserved for the isolation of effector T cells described below. CD62L⁺ cells were flushed out and separated from MultiSort MicroBeads using the MultiSort Release Reagent and centrifugation. CD45RA⁺CD62L⁺ cells were subsequently isolated by negative selection using CD45RO MicroBeads (Miltenyi Biotec, catalogue no. 130-046-001) and two columns (Miltenyi LS). To isolate effector T cells of the same donor as the naive T cells, flowthrough from the first CD62L selection was added to the column (Miltenyi LD) for negative selection of CD62L⁻ cells. More than 95% population purity (determined by flow cytometry) was used in the presented studies. Following isolation, naive and effector cells were electroporated with 10 $\mu\text{g mRNA}/1 \times 10^7$ T cells encoding the CARs using Lonza 4D-Nucleofector Core Unit (pulse code EH115) according to the manufacturer's protocol.

To disrupt the endogenous TCR, T cells were cotransduced with lentiviral CAR constructs and pCAT003, a lentivirus transfer plasmid encoding sgRNA targeting *TRAC* and gift from J. Doudna (Addgene plasmid no. 171628)⁶³. Immediately following debanding, up to 4 $\times 10^6$ T cells were electroporated with 50 pM of Cas9 as described above with the modification of pulse code EO115. TCR⁻ cells were negatively selected using CD3 MicroBeads (Miltenyi Biotec, catalogue no. 130-097-043) and LD column according to the manufacturer's protocol.

To genetically disrupt *IKZF1*, 1 $\times 10^6$ T cells were electroporated immediately following debanding with 50 pM Cas9 and 100 nM guide RNA (IDT, Supplementary Table 2) as described above, with the modification of pulse code EH115. Genomic DNA was isolated using DNeasy Blood & Tissue Kit (Qiagen, catalogue no. 69504) according to the manufacturer's protocol. The targeted *IKZF1* locus was amplified using indicated primers (Supplementary Table 3). Quantification of genetic editing efficiencies were estimated using tracking of indels by decomposition⁶⁴. Western blots were performed and stained using rabbit anti-Ikaros (IKZF1) monoclonal antibody (Cell Signaling, 9034S; dilution 1:1,000), digital antirabbit-HRP (Kindle Biosciences, LLC, R1006; dilution 1:1,000), mouse anti- β -actin monoclonal antibody (Cell Signaling, 3700S; dilution 1:3,000) and digital antimouse-HRP (Kindle Biosciences, LLC, R1005; dilution 1:3,000). Uncropped images of blots are provided in Supplementary Fig. 1. Pharmacologic depletion of *IKZF1* was performed using 0.1 μM lenalidomide (MedChemExpress, catalogue no. HY-A0003).

LIPSTIC assay

Biotinylated LPETG peptide (biotin-amino-hexanoic acid-LPETGS, C-terminal amide, 95% purity)¹⁵ was purchased from LifeTein (custom synthesis), reconstituted in PBS at 10 mM and stored at -80 °C.

To label target cells, Nalm6 cells (expressing sortase-tethered target molecules) were incubated with biotinylated LPETG peptide (100 μM , LifeTein) for 30 min at 37 °C in RPMI/10%FBS, followed by washing three times to remove excess soluble peptide. Sortase-bound LPETG was then

labelled with fluorescent streptavidin (PE, AF647 or APC; $10 \mu\text{g ml}^{-1}$; BioLegend) for 30 min at 37°C . Cells were then washed three times and resuspended at 1×10^6 cells per ml.

All LIPSTIC assays were performed using fully rested T cells that had not demonstrated cell number increases in roughly 2 days. For the CARTs in the presented studies, the transduction efficiencies were between 20 and 85%, and the cell sizes of rested T cells were between 200 and 260 fl, which was achieved 12–15 days after activation. T cells were stained with CellTrace Violet following the manufacturer's recommendations with the following modifications: T cells were stained at a concentration of 1×10^7 cells per ml for 10 min at 37°C . Target cells and CARTs were mixed in a six-well plate well in a total volume of 5.5–7 ml, and CART to target ratios ranged from 0.3:1 to 4.25:1. Cells were incubated for 72 h before cell sorting (BD Biosciences ARIALL) and subsequent analysis of first-division daughter cells.

A second target encounter LIPSTIC assay was performed using sorted first-division LPETG⁺ or LPETG⁻ cells. Target cells labelled with a second colour fluorescent streptavidin and CARTs were mixed in a 96-well plate in a total volume of 200 μl and a 1:1 CART:target ratio. Second-division daughter cells were sorted 24 h after cocultivation.

Sorting gates were established for live single cells that were negative for GFP (excluding target cells), positive for Cell Trace Violet (CTV) and positive or negative for LPETG. LPETG positivity was determined relative to untransduced T cells, CARTs incubated without target cells or irrelevant CARTs incubated with target cells (threshold for LPETG positivity was generally the same for all controls).

Multiparametric flow cytometry analysis of T cells

Unless otherwise specified, antibodies were purchased from BioLegend.

In vitro and in vivo LIPSTIC assay populations were sorted and subsequently phenotyped by staining with 1:200 CD8-APCH7 (SK1, BD Biosciences, catalogue no. 561423), 5:400 CD4-BUV805 (SK3, BD Biosciences, catalogue no. 612887), 1:160 CD45RA-BUV395 (HI100, BD Biosciences, catalogue no. 740298), 5:400 CD45RO (UCHL1, catalogue no. 304234), 1:40 CD25-BV711 (M-A251, catalogue no. 356138) and/or 1:250 CD62L-PE (DREG-56, catalogue no. 304840).

For in vivo studies, samples were stained with CD8-APC/Cy5.5 (RFT8, SouthernBiotech, catalogue no. 9536-18), CD4-PE/Cy5.5 (RFT4, SouthernBiotech, catalogue no. 9522-16), CD3-BV605 (OKT3, catalogue no. 317322), CD19-APC (HIB19, catalogue no. 302212), CD45RA-BUV395 (HI100, catalogue no. 740298), CD45RO-BV785 (UCHL1, catalogue no. 304234), CD62L-PE (DREG-56, catalogue no. 304840), TCR-alpha/beta-BV421 (IP26, catalogue no. 306722) and CD45-PECy7 (QA17A19, catalogue no. 393408) at 1:100 dilution. Whole blood was stained in Trucount tubes (BD Biosciences) and fixed with FacsLyse solution (BD Biosciences) according to the manufacturer's recommendations. Single-cell suspensions from spleen samples were produced by homogenization of the tissue through a 70 μm mesh followed by treatment with Red Blood Cell Lysis Buffer (BioLegend) according to the manufacturer's recommendations and stained in PBS, 1% FBS and cell numbers were quantified with CountBright Plus Absolute Counting Beads (Thermo Fisher).

Samples were analysed on an LSRII, LSR Fortessa or FACSsymphony A3 Cell Analyzer (BD Biosciences). The population of interest was gated based on forward- versus side-scatter characteristics followed by singlet gating. Data were analysed with FlowJo v.10 (Tree Star). Graphs and statistical analyses were generated using GraphPad Prism v.9.4.0.

Live-cell microscopy

For live-cell imaging to capture CARTs undergoing the first cell division, LPETG-positive CARTs before the first cell division were isolated using fluorescence activated cell sorting after 48 h of cocultivation with target cells and then imaged in a humidified incubation chamber at 37°C in 5% CO_2 on a Zeiss Observer 7 equipped with a Zeiss Axiocam

702 monochrome CMOS camera, a Zeiss Axiocam 503 colour CCD camera and a Colibri 7 LED light source in Definite Focus mode in a 35 mm glass bottom dish (Ibidi) every 3 min.

To image the transfer of LPETG peptide from target to CART cells, CTV-labelled T cells were incubated with LPETG peptide-loaded target cells at an effector to target cell ratio of 1:5. The excess of target cells in this context increases the frequency of observing the interaction between CARTs and targets. Cells were placed in a 35 mm glass bottom dish (Ibidi) and analysed in a humidified incubation chamber at 37°C in 5% CO_2 . Photographs were acquired in the GFP, CTV and AF647 channels in Definite Focus mode on a Zeiss Observer 7 every 45 s for 50 min. Images were acquired with $\times 40$ objective using Zen (Blue edition) software (v.2.5, Zeiss). Videos were created with Fiji-ImageJ.

Metabolic analysis

T cell metabolic profiles were assessed using the Seahorse mitochondrial stress test (Agilent Technologies). Individual wells of an XF96 cell-culture microplate were coated with CellTak as per the manufacturer's instructions. The matrix was adsorbed overnight at 37°C , aspirated, air-dried and stored at 4°C until use. Mitochondrial function was assessed on day 0 or day 1 after sorting proximal or distal or undivided cells. T cells were resuspended in non-buffered RPMI 1640 medium containing 5.5 mM glucose, 2 mM L-glutamine and 1 mM sodium pyruvate and seeded at 1.5×10^5 cells per well. The microplate was centrifuged at 1,000g for 5 min and incubated in standard culture conditions for 60 min. During instrument calibration (30 min), the cells were switched to a CO_2 -free 37°C incubator. XF96 assay cartridges were calibrated according to the manufacturer's instructions. Cellular OCRs and ECARs were measured under basal conditions and following treatment with 1.5 μM oligomycin, 1.5 μM FCCP and 40 nM rotenone, with 1 μM antimycin A (XF Cell Mito Stress kit, Agilent). OCR/ECAR ratios are calculated using the mean OCR and ECAR of 3–5 replicates for each population.

In vivo studies

Immunodeficient NSG (NOD.Cg-Prkdc^{scid} Il2rg^{tm1Wjl}/SzJ) mice were bred in house under an approved Institutional Animal Care and Use Committee (IACUC) protocol and maintained under pathogen-free conditions. To facilitate engraftment of T cells, bulk (CD4⁺ and CD8⁺) T cells were used in in vivo studies¹⁹. Sample sizes were not predetermined based on statistical methods but were chosen based on preliminary data and previously published results. For all in vivo experiments, treatment groups were randomly selected by the cage number. In vivo injections were performed in a blinded fashion by a member of the Ellebrecht or Payne laboratories or a staff member of the Human Stem Cell and Xenograft Core of the University of Pennsylvania.

For in vivo LIPSTIC, LPETG-labelled target cells were injected intraperitoneally immediately followed by CTV-labelled CARTs. A 1:1 target:CART ratio was maintained, with a total of 1×10^7 total T cells injected. Mice were euthanized 2 days following injection. Cells were collected using peritoneal wash three times using 5 ml of ice-cold 2% FBS and PBS. First-division daughter cells were sorted and assessed by flow cytometry as described above.

For functional longevity studies, 2.5×10^5 anti-CD19 CAR proximal- or distal-daughter cells, non-activated resting anti-CD19 CARTs or non-transduced T cells were intravenously injected into NSG mice on day 0. After 35 days, mice were challenged with 1×10^6 Nalm6 cells. Leukaemia burden was determined by bioluminescence imaging. Bioluminescence was quantified with an IVIS Lumina III (PerkinElmer) 2–3 times per week after Nalm6 injection as previously described³.

In the stress-test model, NSG mice were injected with 1×10^6 Nalm6 cells on day 0. Engraftment of Nalm6 was confirmed on day 3 by bioluminescence imaging. On day 4, mice were treated with 2.5×10^5 proximal or distal-daughter anti-CD19 CARTs; 2.5×10^6 non-activated resting anti-CD19 CARTs or non-transduced T cells; or 1.3×10^6 bulk

Article

restimulated anti-CD19 CARTs (unsorted) by intravenous injection. Leukaemia burden was determined with bioluminescence imaging as above. Mice were euthanized when they had reached a total bioluminescence flux of at least 1×10^{11} photons per second, demonstrating loss of leukaemia control.

Peripheral blood was obtained by retro-orbital bleeding. Mice were euthanized for organ harvest according to local IACUC guidelines, and spleen and blood samples were assessed by flow cytometry as described above. In accordance with the approved IACUC protocol for these studies, humane endpoints for euthanizing mice were established and not exceeded in this study. Mice were monitored at least twice weekly for symptoms. If severe lethargy or weakness, hunching, emaciated body condition (body condition score of 1 out of 5) or loss of 20% or more body weight, were observed, mice were euthanized. If a body condition score of 2 out of 5 was observed and accompanied by lethargy, mice were euthanized. Furthermore, mice were euthanized when their total bioluminescence flux exceeded 1×10^{11} . All studies involving animals were performed under a protocol approved by the University of Pennsylvania IACUC.

Luciferase-based in vitro cytotoxicity assay

Cytotoxicity assays were performed either on day 1 or 4 after first cell division as previously described³. Click beetle green luciferase-expressing target Nalm6 cells were cocultured with proximal, distal or resting CARTs or donor-matched non-transduced T cells at indicated E:T ratios. To test TCR-mediated cytotoxicity of mRNA-electroporated naive and effector CARTs, K562 cells positive for CD64 (FcγRI) were incubated with $100 \mu\text{g ml}^{-1}$ anti-human CD3 (OKT3, Invitrogen, catalogue no. 16-0037-85) for 30 min on ice and washed twice were used as target cells.

Single-cell multiomic analysis

First-division proximal, first-division distal, activated-undivided and resting CD8 CARTs (1.5×10^5 cells each), sorted as described above from the LIPSTIC assay, were separately incubated in flow cytometry staining buffer (BioLegend) with a custom TotalSeq-C antibody cocktail (Supplementary Table 4, BioLegend 900000114, lot B311489) in $100 \mu\text{l}$ for 30 min at 4°C before washing three times. Cell concentration was adjusted to 1.5×10^6 live cells per ml. 10,000 live CD8 T cells from each LIPSTIC population were loaded onto NextGem K chips (10X Genomics) and processed in a 10X Chromium device according to the manufacturer's recommendations. A biological replicate was performed with CART from a separate donor. Library preparation was performed according to the $10 \times 5'$ V2 protocol for antibody-derived tags (ADT), gene expression (GEX) and paired alpha and beta TCR chains. Complementary DNA and subsequent library intermediates were checked for correct size, appropriate quantity and quality with a DNA high-sensitivity kit on a Bioanalyzer 2100 (Agilent). Libraries were sequenced in paired-end dual-index mode for 150×2 cycles on a NovaSeq 6000 sequencer (Illumina, one lane of a S4 cartridge). All cells in each experiment were sorted and stained on the same day and libraries were processed in parallel and sequenced in the same lane to minimize batch effects. Counts for demultiplexed GEX, ADT and TCR libraries were obtained with the STAR method of the Cell Ranger multi pipeline (10X Genomics, Cell Ranger v.6.1.2) using the human GENCODE v.32/Ensembl 98 GRCh38 reference (detailed version by 10X Genomics: Human (GRCh38) 2020-A, Human (GRCh38) v.5.0.0), which then were aggregated with the Cell Ranger aggr pipeline with read depth normalization to further reduce batch effects across libraries. Downstream analysis was performed with the Seurat V4 R package²². To remove doublets and low cells, cells with more than 25% mitochondrial gene transcripts, less than 7.5% ribosomal gene transcripts, transcript counts less than 500 or greater than 40,000, or a minimum number of detected genes of less than 500 were excluded. Counts were single-cell transformed using the scTransform V2 and glmGamPoi packages⁶⁵.

Dimensionality reduction was performed based on ADT counts with subsequent analysis of genes and surface proteins of interest and differentially expressed genes or surface proteins for T_N , T_{CM} , T_{EM} and T_{RM} -like subsets. RNA velocity analysis was performed by counting spliced and unspliced transcripts in Cell Ranger binary alignment map output files with the velocity package³¹ using the same transcriptome reference gene transfer format file (refdata-gex-GRCh38-2020-A) that was used for the initial Cell Ranger run. Output loom files were then used in scvelo after export of T_N , T_{CM} , T_{EM} and T_{RM} expression matrices containing proximal and distal first-division daughter cells from Seurat and conversion to SCANPY/ANNDATA objects⁶⁶. Global velocity vectors and velocities of genes of interest were computed and visualized in stochastic or dynamic mode with scvelo³⁰. Regulon analysis (gene modules co-expressed with transcription factors and with correct *cis*-regulatory upstream motif for a respective transcription factor) was performed using a list of 1,390 human transcription factors (https://github.com/aertslab/pySCENIC/blob/master/resources/hs_hgnc_curated_tfs.txt) with the Python version of SCENIC (that is, pySCENIC v.0.11.2)^{32,67} after importing expression matrices from Seurat to SCANPY (v.1.7.2). Gene-set enrichment analysis^{68,69} was performed on each T cell subsets with the GSEA function of clusterProfiler⁷⁰ in R. T cell clonal analysis was performed with scRepertoire⁷¹ in R using the 'strict' setting, which requires identical V, D (if applicable), J and C genes in addition to identical CDR3 nucleotide sequence of both TCR chains to identify T cells belonging to the same clonotype.

Seurat analysis was performed in R v.4.3.1, velocity analysis was performed in Python v.3.10.4 and regulon analysis was performed in Python v.3.7.12 in accordance with the respective pipeline requirements.

Statistical analysis

Statistical significance was determined with two-sided tests unless otherwise indicated. Where appropriate and as indicated, *P* values were adjusted for multiple testing (Benjamini–Hochberg). *Q* values were calculated with clusterProfiler in R. Whenever individual data points are presented, a horizontal line represents the mean value of the group. Survival in in vivo experiments was defined as time until the predetermined bioluminescence threshold was reached. Kaplan–Meier statistical analysis was used to compare survival between groups. Unless otherwise indicated, asterisks depict the following significance values: **P* < 0.05, ***P* < 0.01, ****P* < 0.001. *P* values less than 0.05 were considered statistically significant. The mean fluorescence intensity in flow cytometry plots is labelled with a cross in each gate. Statistical analysis was performed with the respective pipelines as mentioned above or with GraphPad Prism v.9.4.0.

Reporting summary

Further information on research design is available in the Nature Portfolio Reporting Summary linked to this article.

Data availability

Single-cell sequencing data have been deposited in the NCBI Gene Expression Omnibus and are accessible through the accession number GSE268878. Source data are provided with this paper.

Code availability

Scripts for single-cell sequencing analysis are available at Zenodo (<https://doi.org/10.5281/zenodo.11672288>)⁷².

59. Littman, D. R. et al. Characterization of an expressed CD3-associated T_H1 gamma-chain reveals C gamma domain polymorphism. *Nature* **326**, 85–88 (1987).
60. Ellebrecht, C. T. et al. Reengineering chimeric antigen receptor T cells for targeted therapy of autoimmune disease. *Science* **353**, 179–184 (2016).
61. Lee, J. et al. Antigen-specific B cell depletion for precision therapy of mucosal pemphigus vulgaris. *J. Clin. Invest.* **130**, 6317–6324 (2020).

62. Zhao, Y. et al. Multiple injections of electroporated autologous T cells expressing a chimeric antigen receptor mediate regression of human disseminated tumor. *Cancer Res.* **70**, 9053–9061 (2010).
63. Hamilton, J. R. et al. Targeted delivery of CRISPR-Cas9 and transgenes enables complex immune cell engineering. *Cell Rep.* **35**, 109207 (2021).
64. Brinkman, E. K., Chen, T., Amendola, M. & van Steensel, B. Easy quantitative assessment of genome editing by sequence trace decomposition. *Nucleic Acids Res.* **42**, e168–e168 (2014).
65. Choudhary, S. & Satija, R. Comparison and evaluation of statistical error models for scRNA-seq. *Genome Biol.* **23**, 27 (2022).
66. Wolf, F. A., Angerer, P. & Theis, F. J. SCANPY: large-scale single-cell gene expression data analysis. *Genome Biol.* **19**, 15 (2018).
67. Aibar, S. et al. SCENIC: single-cell regulatory network inference and clustering. *Nat. Methods* **14**, 1083–1086 (2017).
68. Mootha, V. K. et al. PGC-1 α -responsive genes involved in oxidative phosphorylation are coordinately downregulated in human diabetes. *Nat. Genet.* **34**, 267–273 (2003).
69. Subramanian, A. et al. Gene set enrichment analysis: a knowledge-based approach for interpreting genome-wide expression profiles. *Proc. Natl Acad. Sci. USA* **102**, 15545–15550 (2005).
70. Wu, T. et al. clusterProfiler 4.0: a universal enrichment tool for interpreting omics data. *Innovation* <https://doi.org/10.1016/j.xinn.2021.100141> (2021).
71. Borcherting, N., Bormann, N. L. & Kraus, G. scRepertoire: an R-based toolkit for single-cell immune receptor analysis. *F1000Res.* **9**, 47 (2020).
72. Ellebrecht, C. et al. Fate induction in CD8 chimeric antigen receptor T-cells through asymmetric cell division. Zenodo <https://doi.org/10.5281/zenodo.11672288> (2024).

Acknowledgements We thank W. Wilson for bioinformatics discussion, A. Stout from the Cell and Developmental Biology Microscopy Core for assistance with imaging experiments, and the Penn Stem Cell and Xenograft Core. Flow cytometry and sorting were performed in the Penn Cytomics and Cell Sorting Shared Resource Laboratory at the University of Pennsylvania, supported by the Abramson Cancer Center NCI grant (no. P30 016520, the research identifier number is RRid:SCR_022376). We thank E. Cento, Z. Chen, M. A. Eldabbas and E. Maddox of the Human Immunology Core (HIC) and the Division of Transfusion Medicine and Therapeutic Pathology at the Perelman School of Medicine at the University of Pennsylvania for providing de-identified, bulk T cells and CD8⁺ T cells that were purified from healthy donor apheresis using StemCell RosetteSep kits. The HIC is supported in part by grant nos. NIH P30 A1045008

and P30 CA016520. HIC RRID: SCR_022380. Research reported in this publication was supported by the National Institute of Arthritis and Musculoskeletal and Skin Diseases and National Cancer Institute of the National Institutes of Health through grant awards to C.T.E. (grant no. K08-AR0802666, Dermatology Foundation Career Development Award), C.S.L. (grant no. T32-AR007465), S.O. (National Research Foundation of Korea, funded by the Ministry of Education, grant no. 2019R1A6A3A03033057), R.O.C. (grant no. R01-CA226983, Ludwig Princeton Branch) and A.S.P. (grant no. R01-AR068288, Penn Center for Precision Medicine). The content is solely the responsibility of the authors and does not necessarily represent the official views of the National Institutes of Health.

Author contributions A.R.K. assisted with experiments and manuscript review. A.S.P. was involved with experimental design, supervision of experimental execution and data analysis, and manuscript writing. C.T.B. performed bioinformatics analysis and reviewed the manuscript. C.T.E. was involved with experimental design and execution, experimental data and bioinformatics analysis, manuscript writing, supervision of experimental execution and data analysis. C.S.L. was involved with experimental design and execution, experimental data analysis and manuscript writing. P.J.H. assisted with experiments and manuscript review. R.O.C. was involved with experimental design, supervision of experimental execution and data analysis, and manuscript review. S.C. was involved with experimental design and execution, experimental data analysis and manuscript review. S.O. assisted with experiments and manuscript review.

Competing interests C.T.E.—equity (Cabaletta Bio), patent licensing (Cabaletta Bio, Novartis). A.S.P.—equity, payments, research grants (Cabaletta Bio), patent licensing (Cabaletta Bio, Novartis), consultant (Janssen). S.O.—patent licensing (Cabaletta Bio). R.O.C.—equity (Nucleus Biologics), research grant (NeoTx) and patent licensing (Novartis). The remaining authors declare no competing interests.

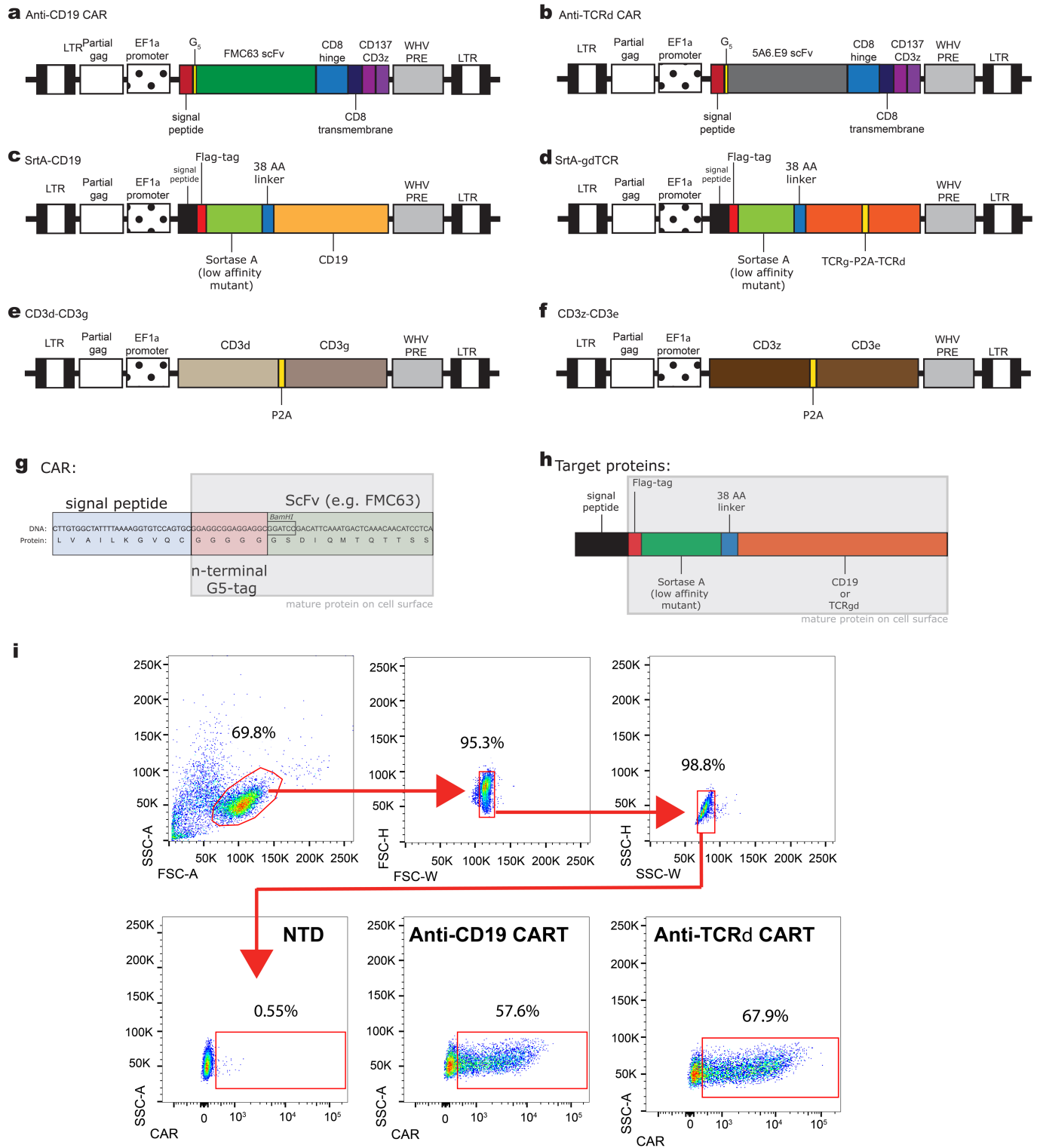
Additional information

Supplementary information The online version contains supplementary material available at <https://doi.org/10.1038/s41586-024-07862-7>.

Correspondence and requests for materials should be addressed to Aimee S. Payne or Christoph T. Ellebrecht.

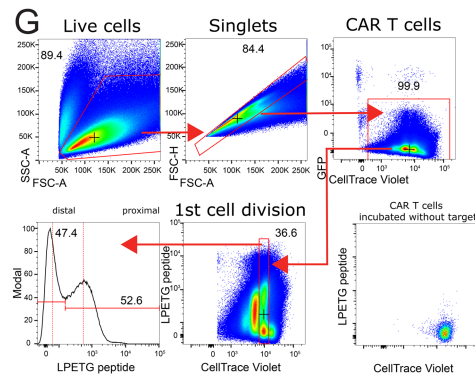
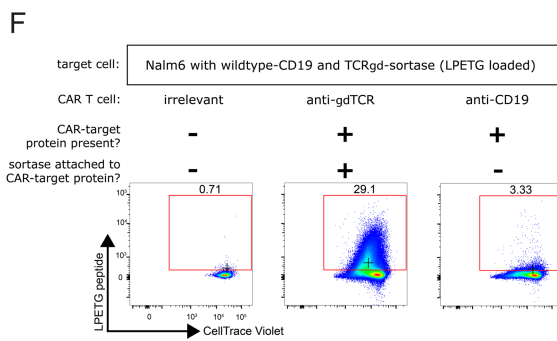
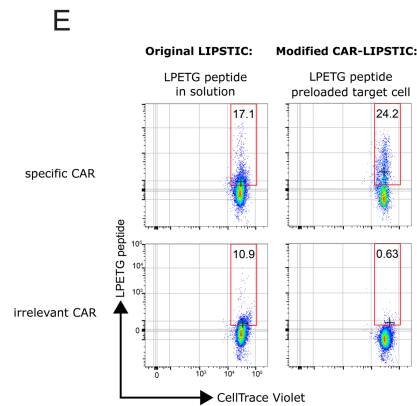
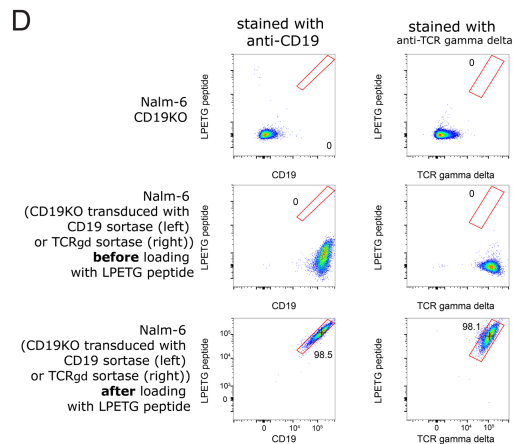
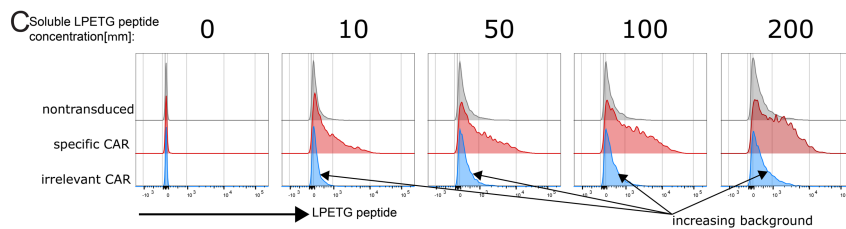
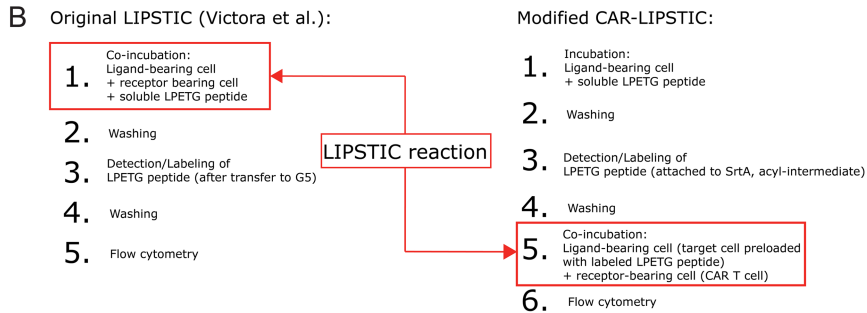
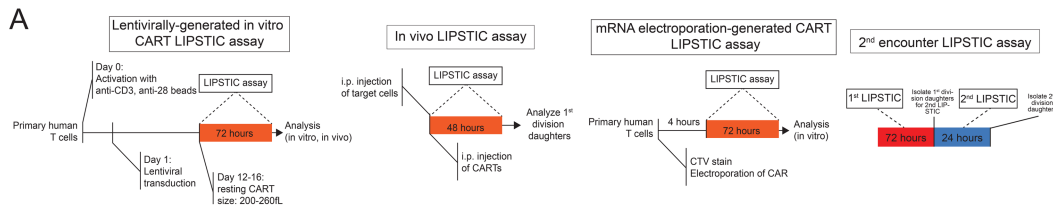
Peer review information *Nature* thanks Stephen Gottschalk and the other, anonymous, reviewer(s) for their contribution to the peer review of this work.

Reprints and permissions information is available at <http://www.nature.com/reprints>.



Extended Data Fig. 1 | Schematics of CAR and target protein lentiviral constructs. **a**, N-terminal pentaglycine (G_5) anti-CD19 CAR (clone FMC63). **b**, N-terminal pentaglycine anti-TCR δ CAR (clone: 5A6.E9). **c**, Sortase-A linked CD19. **d-f**, Sortase-A linked TCR γ with TCR δ (**d**); CD3 δ and CD3 γ (**e**); and CD3 ζ and CD3 ϵ (**f**) for generating sortase-A linked $\gamma\delta$ TCR target cells. **g**, Nucleotide and amino acid sequence of the N-terminus of CAR constructs showing the signal peptide, pentaglycine tag, and N-terminal portion of the anti-CD19 scFv.

Gray rectangle indicates start of mature protein sequence. **h**, Schematic of sortase-A linked target protein; gray rectangle indicates mature protein. **i**, Representative flow staining of surface G_5 anti-CD19 CAR and G_5 anti-TCR δ CAR. LTR, long terminal repeat; scFv, single chain variable fragment; WHV PRE, woodchuck hepatitis virus post-transcriptional regulatory element; SrtA, sortase-A. Sequences of displayed constructs can be found in Supplementary Table 1.

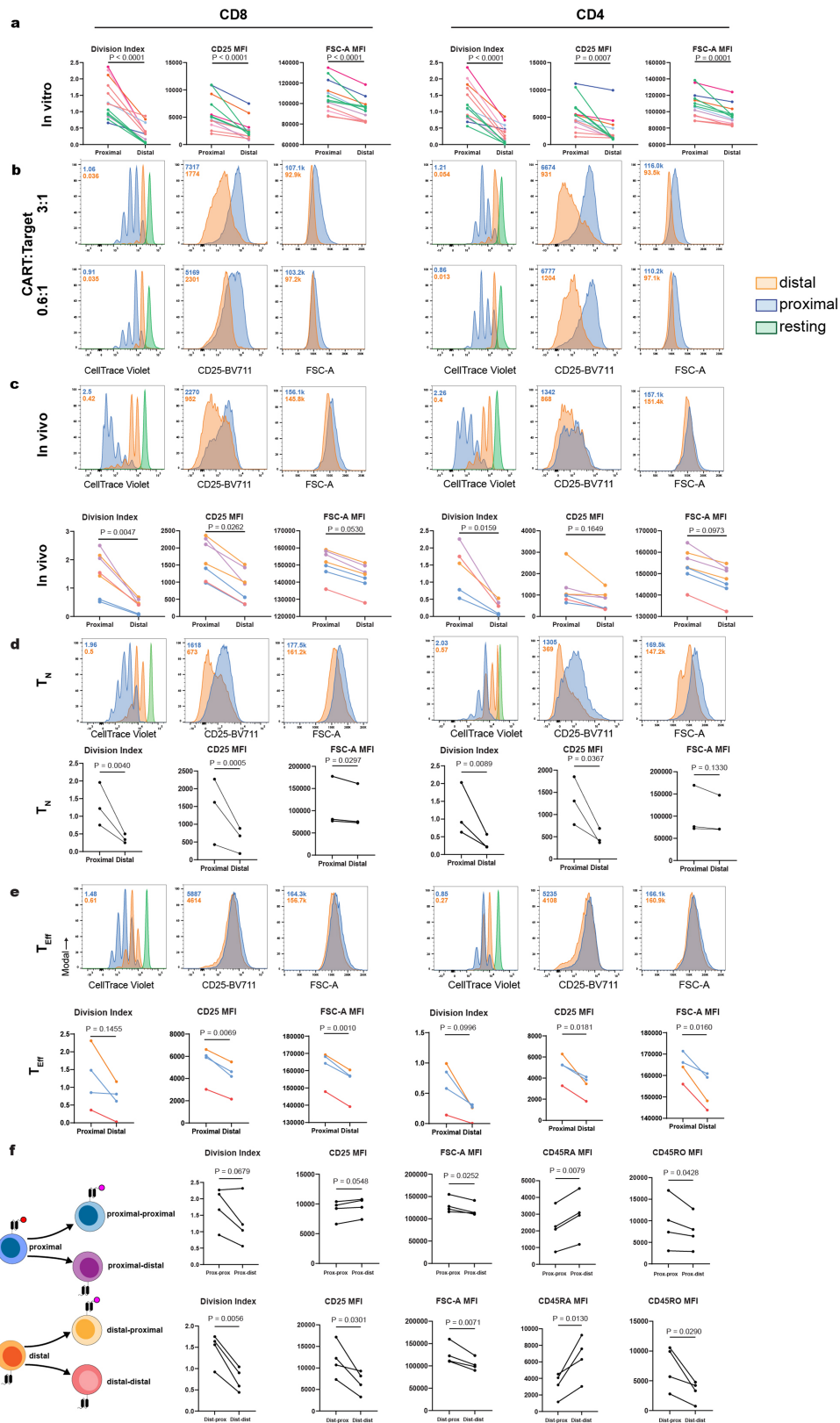


Extended Data Fig. 2 | See next page for caption.

Article

Extended Data Fig. 2 | Modified LIPSTIC assay specifically labels proximal-daughter CARTs using sortase-A linked target. **a**, Timeline of lentivirally-transduced CART in vitro and in vivo LIPSTIC assay, electroporated CART in vitro LIPSTIC assay (for T_N and T_{Eff} CART experiments), and second target encounter LIPSTIC assay. **b**, Comparison of previously described LIPSTIC and modified CAR-LIPSTIC protocols for specific labeling and sorting of proximal versus distal daughter CARTs. In the modified CAR-LIPSTIC approach, ligand-bearing target cells with sortase-A are incubated ('preloaded') with soluble biotinylated LPETG peptide, washed, and subsequently stained with streptavidin-fluorophore to detect LPETG peptides attached to sortase-A. Labeled target cells are co-incubated with CART cells, and LIPSTIC labeling of CAR molecules is analyzed by flow cytometry. **c**, Titration of soluble LPETG peptide concentration using the previously described LIPSTIC assay demonstrates increasing non-specific signal on nontransduced T cells and irrelevant CART T cells with increasing LPETG peptide concentration (gated on live, singlet cells). **d**, Flow cytometry plots (gated on live, singlet cells) demonstrating the expression of sortase-A linked target protein (CD19 or

$\gamma\delta$ TCR) and co-detection of LPETG peptide and sortase-A linked target proteins before and after LPETG peptide incubation. **e**, Flow cytometry plots (gated on live, singlet cells) showing increased LPETG label detection on target-specific CAR and decreased LPETG background labeling on irrelevant CAR when using the modified CAR-LIPSTIC approach compared to the previously described LIPSTIC approach. **f**, Flow cytometry plots demonstrating specific labeling of CAR targeting sortase-A linked target protein. Anti-CD19 and anti- $\gamma\delta$ TCR CAR T cells proliferate (determined by CellTrace Violet dilution) when co-incubated with wild-type CD19- and $\gamma\delta$ TCR-sortase-expressing Nalm6 cells, but only the anti- $\gamma\delta$ TCR CAR is labeled with the LPETG peptide after co-incubation. This demonstrates that LIPSTIC labeling is proximity sensitive, i.e. CART interaction with sortase-positive cells (where sortase is attached to a surface protein that is not in proximity to the CAR target) is not sufficient to label CARs; instead, the sortase enzyme has to be attached to the CAR target in order to facilitate labeling. **g**, Gating strategy for the discrimination of first-division proximal- and distal-daughter CARTs.

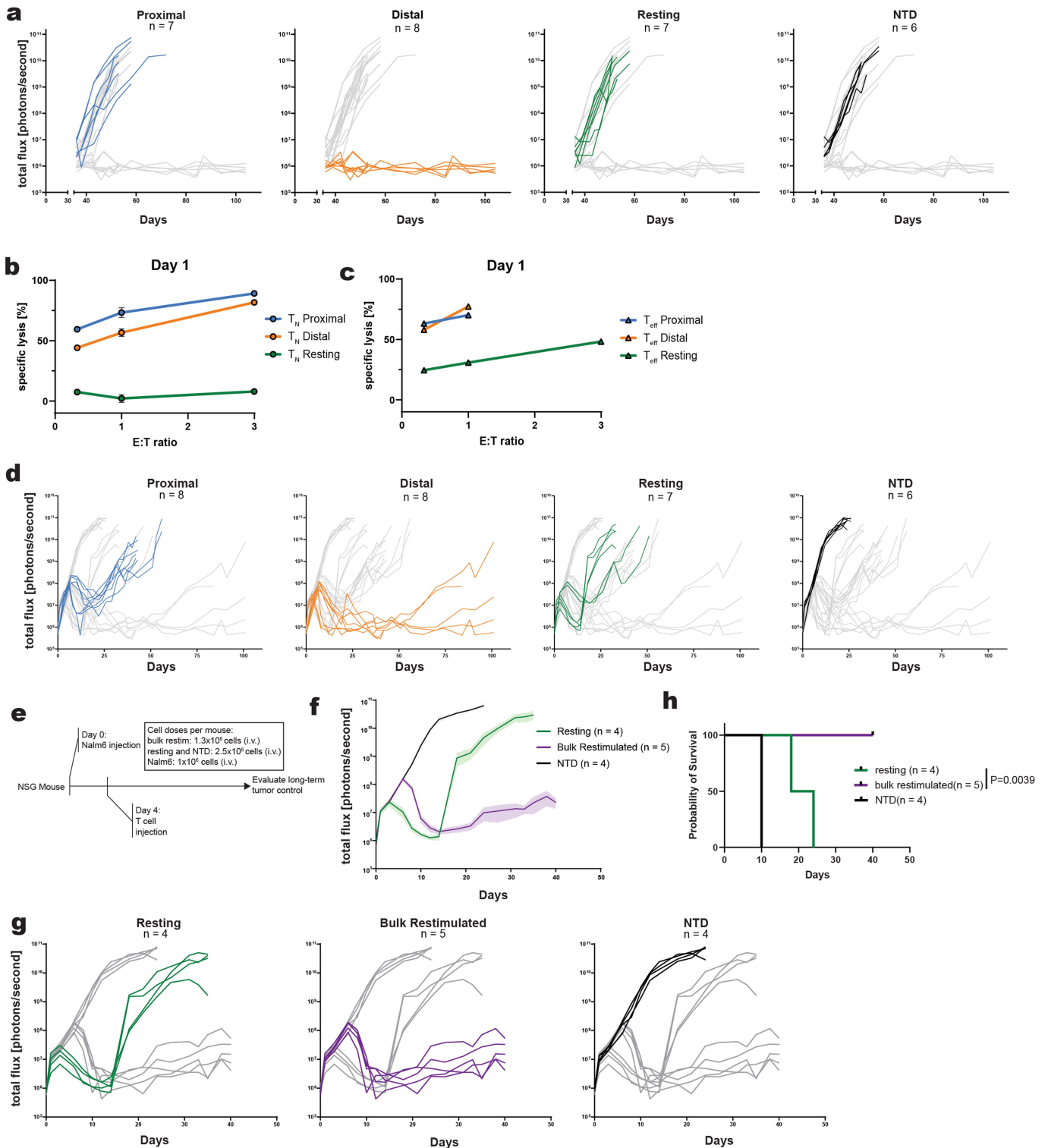


Extended Data Fig. 3 | See next page for caption.

Article

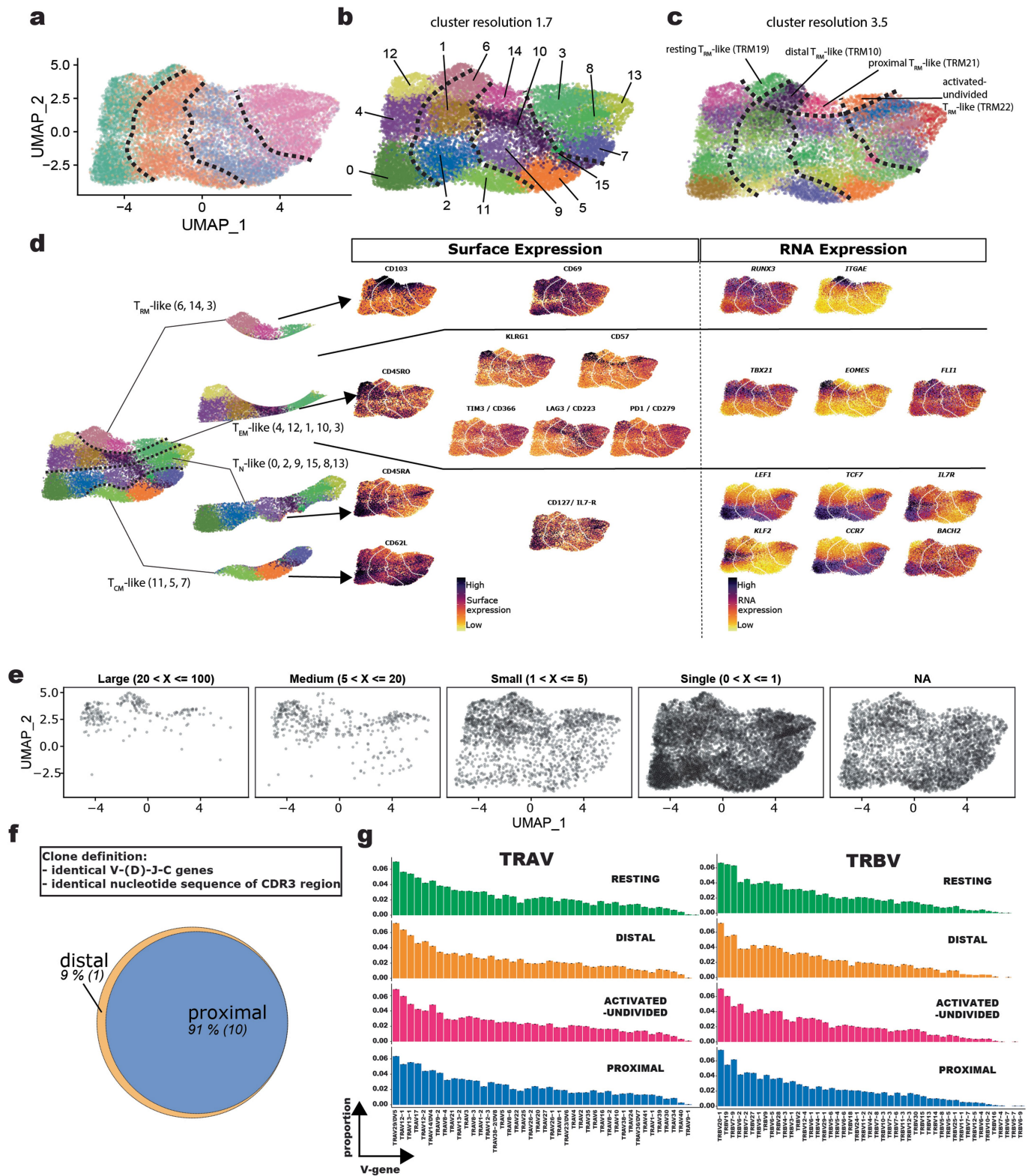
Extended Data Fig. 3 | CART subsets exhibit ACD following first and second target encounter. a-d, Representative flow cytometry histograms and summary statistics of CD8 (left) and CD4 (right) proximal-daughter and distal-daughter CART progeny 3 days after first-division daughter cell isolation. **(a)** Summary of in vitro LIPSTIC assays (n = 13, 8 distinct donors), **(b)** First-division daughters isolated after LIPSTIC assay cocubation using 3:1 or 0.6:1 CART:target ratio in vitro, **(c)** first-division daughters isolated after in vivo activation (n = 5 for CD4 Division Index, n = 7 for other measurements, 4 distinct donors), **(d)** first-division daughters isolated from CARTs generated in vitro from T_N cells (n = 3 from distinct donors), **(e)** first-division daughters isolated from CARTs generated

in vitro from T_{eff} cells (n = 4, 3 distinct donors). **f**, Division index or median fluorescence intensity of CD8 proximal-proximal, proximal-distal, distal-proximal, and distal-distal daughter CART progeny 2 days after second-division daughter cell isolation (n = 4 from distinct donors). CD8 cells were gated on CTV⁺CD8⁺ singlets, and CD4 cells were gated on CTV⁺CD4⁺ singlets. In **(b)**, **(c)**, and **(e)**, each color within the same panel represents a distinct donor, with the same colors representing technical replicates, and in **(d)** and **(f)**, each connected pair represents a distinct donor. Data from both anti-TCR δ CARTs and anti-CD19 CARTs are combined. Statistical significance was determined using two-tailed ratio paired t-test.



Extended Data Fig. 4 | First-division daughter and bulk restimulated CARTs exhibit potent tumor lysis and in vivo tumor control. **a**, Bioluminescence imaging quantification of Nalm6 cells in NSG mice depicted in Fig. 2c by treatment group (n = 6–8 mice per treatment group pooled from 3 independent experiments). **b-c**, 20-hour in vitro cytotoxicity data of proximal-daughter, distal-daughter, and resting CARTs 1 day after first cell division of (**b**) T_N -derived or (**c**) T_{eff} -derived CARTs. Data points represent the mean (n = 3 replicates for all groups except n = 2 replicates for T_{eff} proximal and distal) and error bars represent standard error of the mean in (**b**). **d**, Bioluminescence imaging quantification of Nalm6 cells in NSG mice depicted in Fig. 3c by treatment group (n = 6–8 mice

per treatment group pooled from 3 independent experiments). **e**, Experimental design evaluating acute tumor control of bulk restimulated CARTs, resting CARTs, and NTD. **f-g**, Bioluminescence imaging quantification of Nalm6 cells in the NSG mouse model. In **f**, lines represent means and shaded areas represent standard error of the mean. **h**, Kaplan–Meier survival curve. Dashes indicate censored data. (**f-h**) n = 4–5 mice per treatment group from one experiment, with NTD and resting conditions constituting a subset of replicates displayed in Fig. 3c and Extended Data Fig. 4d. Statistical significance was determined using a log-rank test in (**g**).

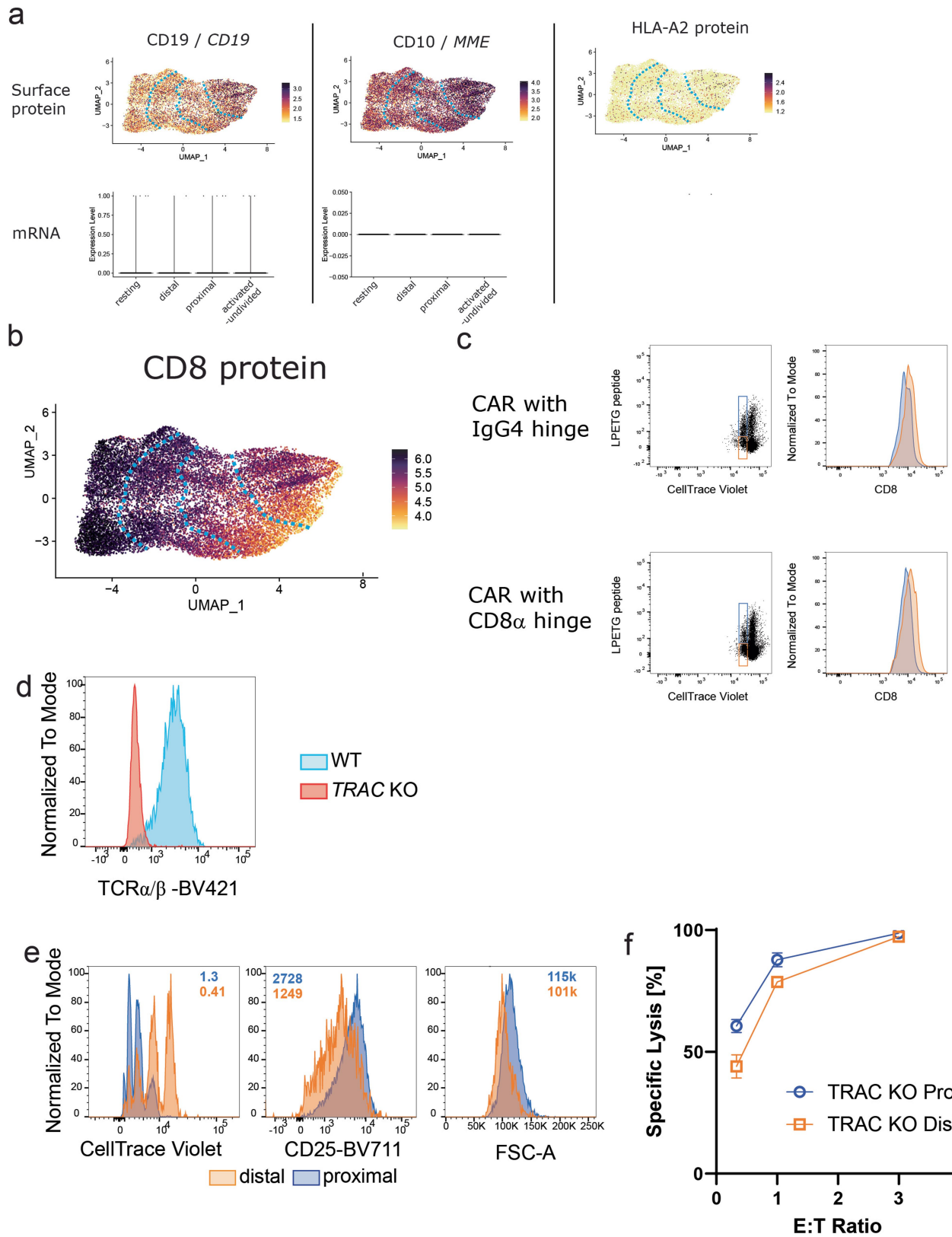


Extended Data Fig. 5 | See next page for caption.

Extended Data Fig. 5 | Simultaneous surface proteomic and transcriptional profiling reveals CD8⁺ CART subsets, expanded T-cell clones in effector subsets, and clonal overlap between proximal- and distal-daughter CARTs.

a, UMAP plot using surface protein expression colored by LIPSTIC-sorted cell population. **b-c**, Unsupervised clustering of UMAP plot using **(b)** cluster resolution 1.7 and **(c)** cluster resolution 3.5. **d**, Using cluster resolution 1.7, clusters were assigned to T_N-like (expression of CD45RA, CD62L, IL7-R, *TCF7*, *LEF1*, *CCR7*, *KLF2*, and *BACH2*), T_{CM}-like (expression of CD62L, CD45RO, *LEF1*, *CCR7*, and absence of CD45RA), T_{EM}-like (expression of CD45RO, KLRG1, *CD57*, *TBX21*, *EOMES*, *FLI1* and *RUNX3* and absence of CD62L), and T_{RM}-like (expression of CD103, CD69, *ITGAE*, and *RUNX3*) subsets using surface protein and gene expression. UMAP plots identical to Fig. 5a (shown here for subset identification).

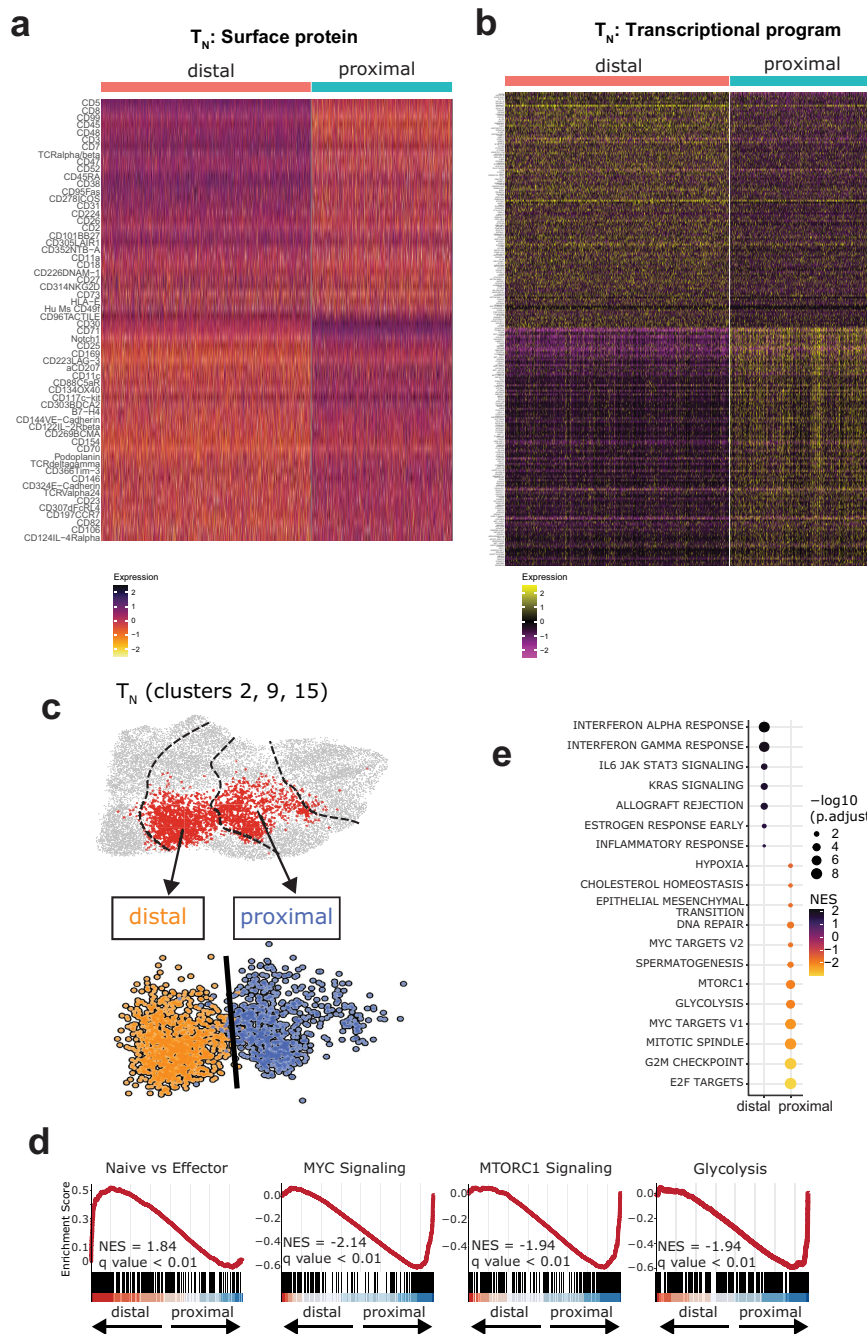
e, UMAP plot based on the size of each cell's clonotype. Clonotype is defined by identical V, D (if applicable), J, and C genes in addition to identical CDR3 nucleotide sequences on both the TCR α and TCR β chains. The large and medium clonotypes were predominantly detected in T_{RM}- and T_{EM}-like clusters. **f**, Venn diagram showing the overlap of the top 10 expanded clonotypes in proximal daughters and their overlap with distal-daughter clonotypes. Of the 11 expanded clonotypes detected across proximal- and distal-daughter populations, 10 clonotypes are detected in both first-division daughter cell populations. **g**, Proportion of *TRAV* and *TRBV* gene usage in resting, distal, activated-undivided, and proximal CARTs. V-gene usage is similar across the T-cell groups, without notable V-gene skewing.



Extended Data Fig. 6 | See next page for caption.

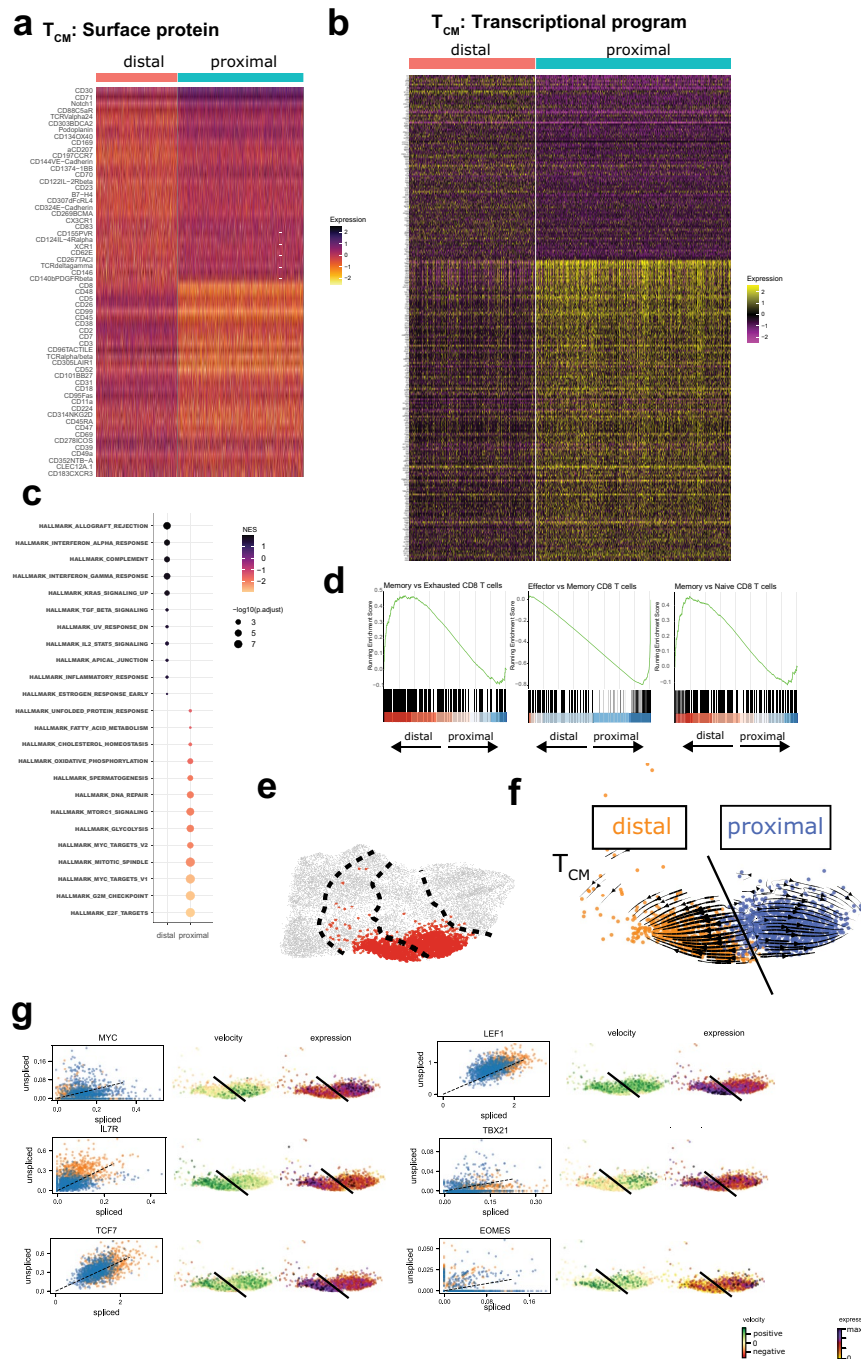
Extended Data Fig. 6 | Simultaneous surface protein and gene expression detection demonstrates trogocytosis of B-cell-associated proteins from Nalm6 target cells to CARTs and surface CD8 enrichment in first-division distal-daughter CARTs. **a**, Normalized B-cell-associated CD19 and CD10 protein detection on CARTs is displayed on UMAP plots in the top row, and normalized gene expression levels for these proteins in resting, distal, proximal, and activated-undivided CARTs are plotted in the bottom row. Absence of gene expression but detection of surface proteins supports transfer of these proteins from target cells to CARTs. HLA-A2 serves as isotype control. **b**, Normalized surface expression of CD8 displayed on UMAP plot demonstrating enrichment of CD8 on resting and distal-daughter CARTs over activated-undivided and proximal-daughter CARTs. **c**, Distal-daughter CARTs isolated when using CAR

constructs with either an IgG4 hinge or a CD8 α hinge demonstrate higher CD8 surface levels by flow cytometry compared to proximal-daughter CARTs. Cells are pregated on singlet cells. **d**, TCR α/β surface expression of WT or *TRACKO* T cells. Cells are pregated on singlet cells. **e**, Flow cytometry histograms of proximal-daughters and distal-daughters generated from CD8 *TRACKO* CARTs 3 days following first-division daughter cell isolation. Cells are gated on singlet CD8⁺ cells. **f**, In vitro cytotoxicity assay of bulk *TRACKO* proximal-daughter and distal-daughter performed within one day after isolation of first-division daughter CARTs. Data points represent mean of triplicates, error bars represent standard deviation. Plots representative of 2–3 independent experiments with CARTs from distinct donors.



Extended Data Fig. 7 | T_N -like proximal-daughter and distal-daughter CD8 CARTs exhibit asymmetry in surface proteomic and transcriptional landscapes that drive differentiation and metabolic programs. a-b, Heat maps for first-division T_N -like CARTs of **(a)** normalized surface protein levels of the top 30 proteins enriched in either distal-daughter (top half) or proximal-daughter (bottom half) T_N -like CARTs and **(b)** normalized gene expression of top enriched genes in distal-daughter (top half) and in proximal-daughter (bottom half) T_N -like CARTs demonstrate asymmetry in surface proteome and transcriptional abundance between first-division proximal-daughter and distal-daughter T_N -like CARTs. **c,** Proximal-daughter and distal-daughter CD8 T_N clusters (2, 9, 15) characterized in Fig. 5c, d. **d,** Gene-set enrichment plots

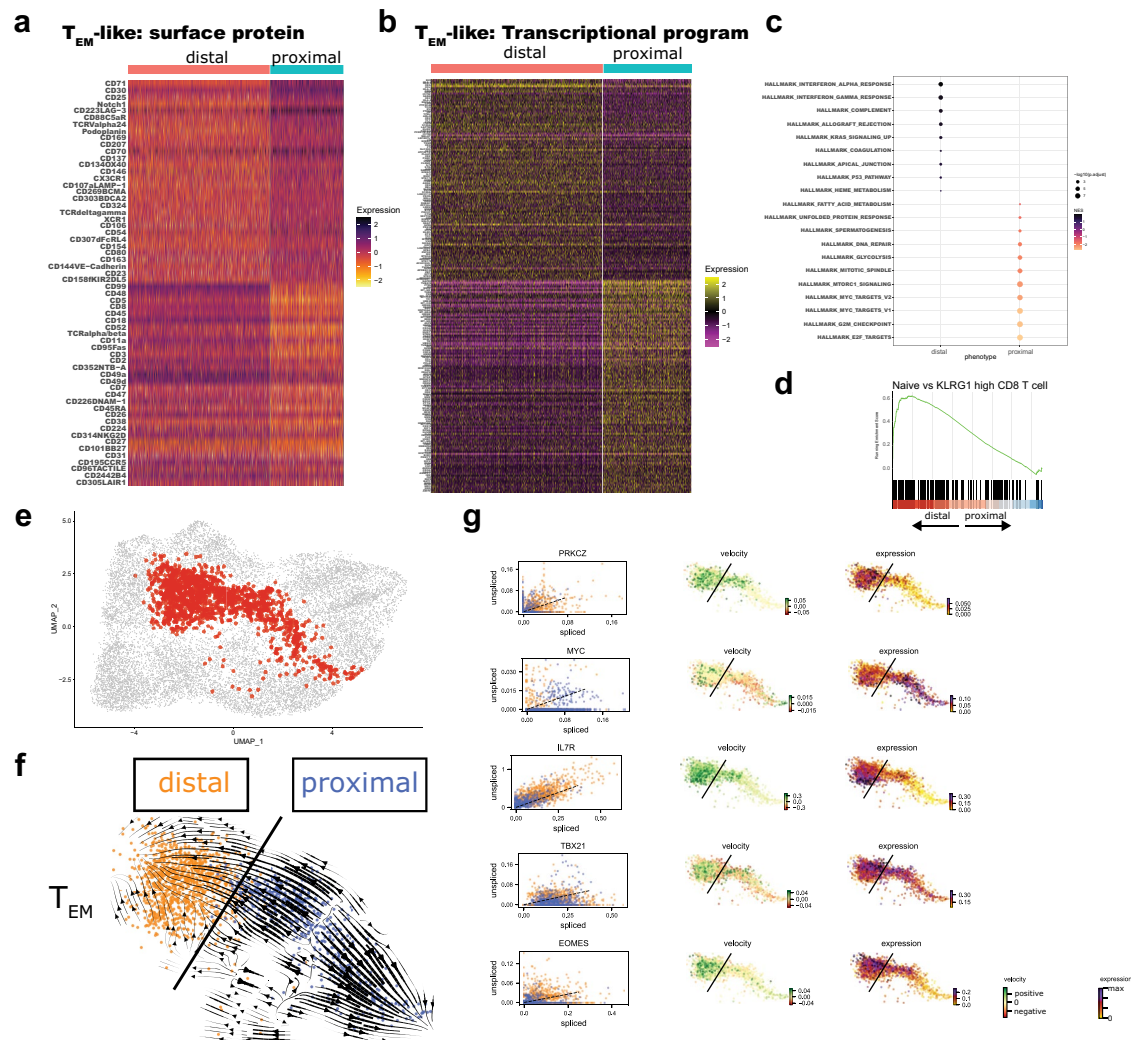
comparing transcriptional programs of proximal-daughter and distal-daughter T_N -like CD8 CARTs, indicating enrichment of naïve-associated genes in distal-daughter T_N -like CD8 CARTs (positive enrichment score values) and enrichment of genes associated with MYC, MTORC1 signaling, and glycolysis in proximal-daughter T_N -like CD8 CARTs (negative enrichment score values). **e,** Hallmark transcriptional programs of proximal-daughter and distal-daughter T_N -like CARTs. Statistical significance was determined using GSEA test with Benjamini-Hochberg correction for multiple comparisons. Plots are representative of 2 independent experiments with distinct donors: one with the anti-TCR δ CAR (shown in this figure) and one with the anti-CD19 CAR.



Extended Data Fig. 8 | T_{CM} -like proximal-daughter and distal-daughter CD8 CARTs exhibit asymmetry in surface proteomic and transcriptional landscapes that drive effector or memory differentiation programs.

a-h, Surface proteomic and transcriptional profile asymmetry in first-division T_{CM} -like daughter CARTs support memory maintenance in distal cells and proliferative and effector differentiation in proximal cells. **(a)** Heat map of normalized surface protein levels of the top 30 proteins enriched in either distal or proximal cells. **(b)** Heat map of normalized gene expression of top enriched genes in distal-daughters (180 genes) and proximal-daughters (240 genes). **(c)** Hallmark transcriptional programs of distal and proximal T_{CM} -like CARTs support increased metabolic activity (fatty acid metabolism, oxidative phosphorylation, glycolysis, MTORC1 signaling) and proliferation (MYC targets, mitotic spindle, G2M checkpoint, E2F targets) in proximal-daughters compared to distal-daughters. Statistical significance was determined using GSEA test with Benjamini–Hochberg correction for multiple comparisons. **(d)** Gene-set enrichment plots comparing transcriptional programs between distal-daughter

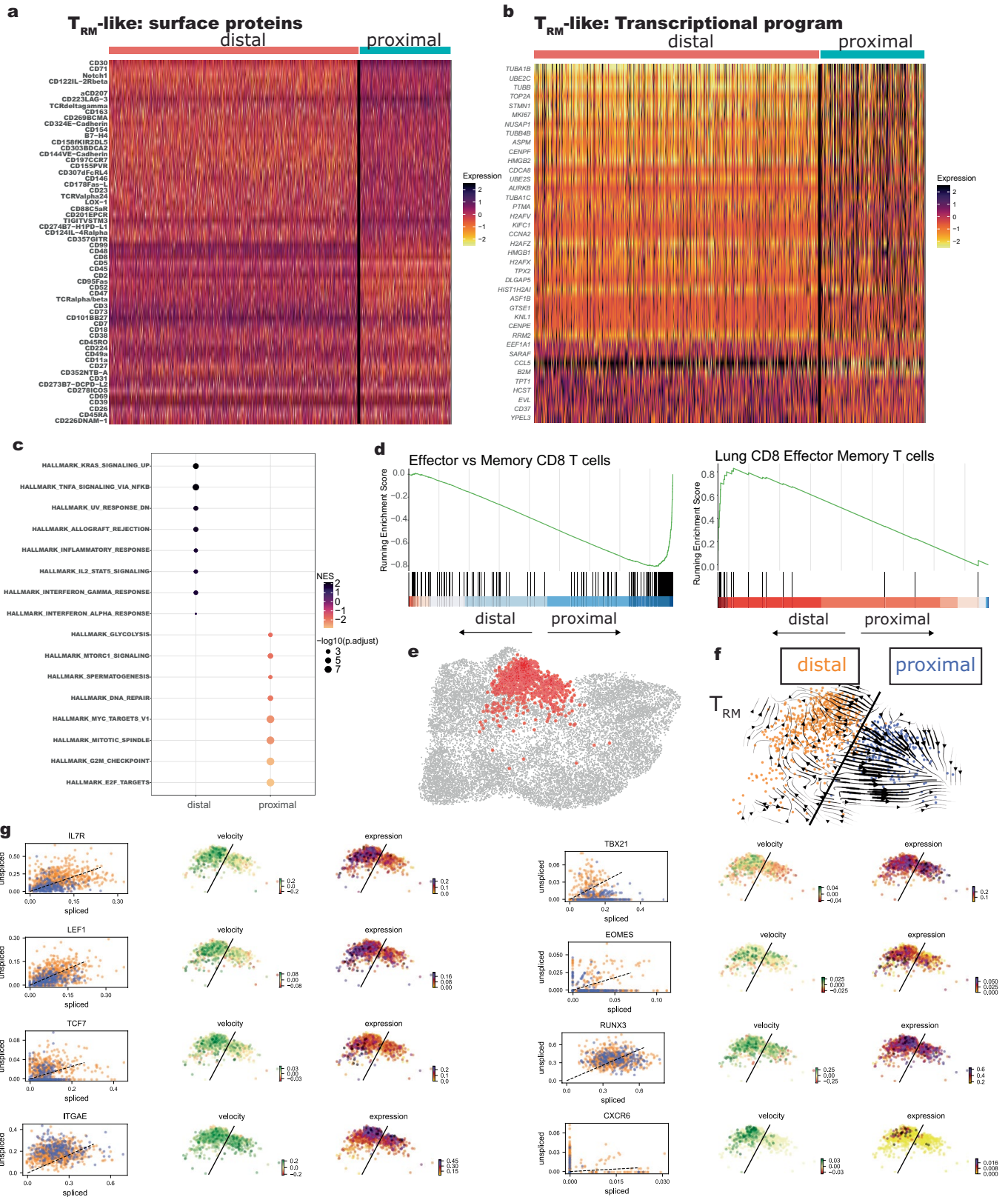
and proximal-daughter T_{CM} -like CARTs demonstrating enrichment in memory-associated programs in distal cells and effector-associated programs in proximal cells. **(e)** Proximal and distal T_{CM} clusters (clusters 11 and 5) characterized in **f-g**. **(f)** Velocity vector projection onto T_{CM} UMAP clusters with streamline plots indicating divergent cell-state transitions between proximal and distal daughter cells. Black line signifies border between distal (orange) and proximal (blue) cells. **(g)** Gene-specific RNA velocity displayed as spliced/unspliced transcripts (left column) and projected onto T_{CM} UMAP clusters (middle column), with normalized gene expression levels as a comparison (right column), demonstrate that both intrinsic transcriptional changes (*MYC* upregulation in proximal-daughters, *IL7R* upregulation in distal-daughters) and asymmetric assortment of pre-existing RNA (greater abundance of *TCF7*, *LEF1* in distal-daughters with similar RNA velocities as proximal-daughters) are mechanisms for transcript abundance differences during ATCD. Plots are representative of 2 independent experiments with distinct donors: one with the anti-TCR CAR (shown in this figure) and one with the anti-CD19 CAR.



Extended Data Fig. 9 | Surface proteomic and transcriptional asymmetry between proximal-daughter and distal-daughter T_{EM} -like CD8 CARTs.

a-b, Heat maps of (a) normalized surface protein levels of the top 30 proteins enriched in either distal-daughters or proximal-daughters and (b) normalized gene expression of top enriched genes in distal-daughters and in proximal-daughters demonstrate asymmetry in surface proteome and transcriptional abundance between first-division proximal-daughter and distal-daughter T_{EM} -like CARTs. **c**, Hallmark transcriptional programs of distal and proximal T_{EM} -like CARTs support interferon alpha and gamma response in distal-daughters and increase metabolic activity (glycolysis, MTORC1 signaling) and proliferation (MYC targets, mitotic spindle, G2M checkpoint, E2F targets) in proximal-daughters. Statistical significance was determined using GSEA test with Benjamini–Hochberg correction for multiple comparisons. **d**, Gene-set enrichment plot between distal-daughter and proximal-daughter T_{EM} -like CARTs demonstrate enrichment of naive-associated programs rather than KLRG1^{hi} effector cell-associated programs in distal-daughters. **e**, Proximal and distal T_{EM} clusters (clusters 10 and 1) characterized in **f-g**. **f**, Velocity vector projection onto T_{EM} UMAP clusters with streamline plots indicating divergent

cell-state transitions between distal-daughters and a portion of proximal-daughters. A subset of proximal-daughters exhibit velocity vectors with the same directionality as that of distal-daughters, which may reflect heterogeneity in T_{EM} -like proximal-daughters, with a fraction of proximal-daughters exhibiting a trajectory toward a memory-like rather than effector-like cell state. Black line signifies border between distal (orange) and proximal (blue) cells. **g**, Gene-specific RNA velocity displayed as spliced/unspliced transcripts (left column) and projected onto T_{EM} UMAP clusters (middle column), with normalized gene expression levels as a comparison (right column) demonstrating that, consistent with prior reports, *PRKCZ* transcripts are enriched in distal-daughters and *MYC* transcripts are enriched in proximal-daughters. Consistent with the velocity vector projection in **f** and similar to distal-daughters, a portion of proximal-daughters upregulate and exhibit higher transcript abundance of *PRKCZ* and *IL7R* transcription. Similar to T_N and T_{CM} cells, *MYC*, *IL7R*, and *TBX21* demonstrate velocity changes in first division daughter cells indicative of asymmetric intrinsic transcriptional changes of these genes. Plots are representative of 2 independent experiments with distinct donors: one with the anti-TCR δ CAR (shown in this figure) and one with the anti-CD19 CAR.

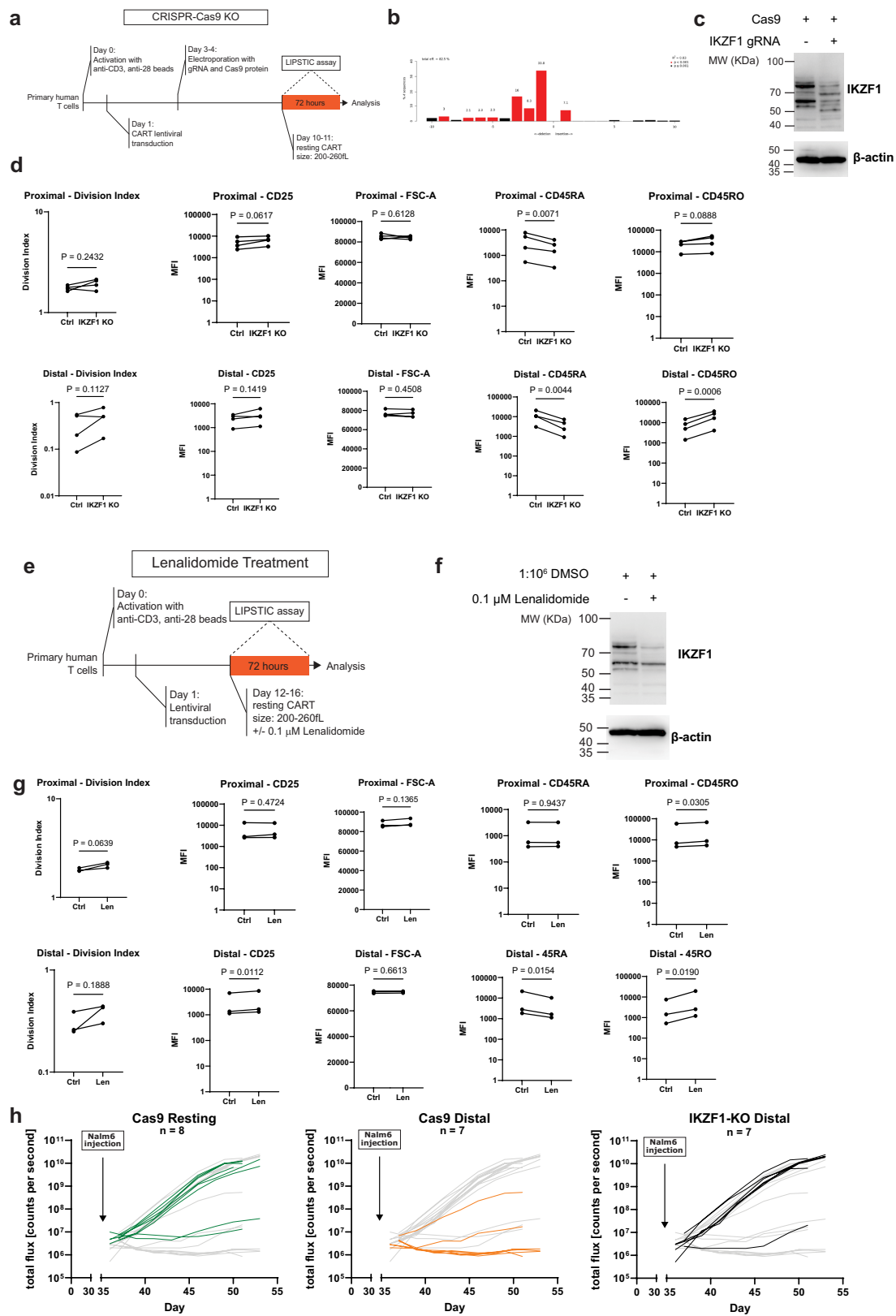


Extended Data Fig. 10 | See next page for caption.

Article

Extended Data Fig. 10 | Surface proteomic and transcriptional asymmetry between first-division proximal-daughter and distal-daughter T_{RM}-like CD8 CARTs. **a-b**, Heat map of **(a)** normalized surface protein levels of the top 30 proteins enriched in either distal-daughters or proximal-daughters and **(b)** normalized gene expression of top enriched genes in either distal-daughters or proximal-daughters demonstrate asymmetry in surface proteome and transcriptional abundance between first-division proximal-daughter and distal-daughter T_{RM}-like CARTs. **c**, Hallmark transcriptional programs of distal and proximal T_{RM}-like CARTs support interferon alpha and gamma response in distal-daughters and increase metabolic activity (glycolysis, MTORC1 signaling) and proliferation (MYC targets, mitotic spindle, G2M checkpoint, E2F targets) in proximal-daughters. Statistical significance was determined using GSEA test with Benjamini-Hochberg correction for multiple comparisons. **d**, Gene-set enrichment plot between distal and proximal T_{RM}-like CARTs demonstrate

enrichment of lung effector memory cell-associated programs in distal-daughters and effector cell-associated programs in proximal-daughters. **e**, Proximal and distal T_{RM} clusters (clusters TRM21 and TRM10) characterized in F-g. **f**, Velocity vector projection onto T_{RM} UMAP clusters with streamline plots indicating divergent cell-state transitions between proximal-daughters and distal-daughters. Black line signifies border between distal (orange) and proximal (blue) cells. **g**, Gene-specific RNA velocity displayed as spliced/unspliced transcripts (left column) and projected onto T_{RM} UMAP clusters (middle column), with normalized gene expression levels as a comparison (right column) demonstrating intrinsic upregulation of *IL7R*, *LEF1*, *TCF7*, and *CXCR6* in distal-daughters compared to proximal-daughters. Plots are representative of 2 independent experiments with distinct donors: one with the anti-TCR δ CAR (shown in this figure) and one with the anti-CD19 CAR.



Extended Data Fig. 11 | See next page for caption.

Article

Extended Data Fig. 11 | IKZF1 downregulation promotes effector-like differentiation of distal-daughter CARTs. **a**, Experimental timeline of *IKZF1*-KO CART generation and subsequent LIPSTIC assay. **b**, Representative Tracking of Indels by Decomposition (TIDE) analysis of two independent experiments to calculate the rate of *IKZF1* gene editing. **c**, Representative western blot of two independent experiments detecting IKZF1 and β -actin of Cas9 control and *IKZF1*-KO CARTs. **d**, Flow cytometry summary statistics comparing proximal- and distal-daughter progeny of Cas9 control and *IKZF1*-KO CARTs (n = 4 independent experiments with distinct donors). **e**, Bioluminescence imaging

quantification of Nalm6 cells in NSG mice related to Fig. 5g–j by treatment group (n = 7–8 mice per treatment group pooled from 2 independent experiments). **f**, Experimental timeline of IKZF1 depletion with use of lenalidomide and subsequent LIPSTIC assay. **g**, Representative western blot of two independent experiments detecting IKZF1 and β -actin of CARTs treated with DMSO or 0.1 μ M lenalidomide for 1 day. **h**, Flow cytometry summary statistics comparing proximal- and distal-daughter progeny of DMSO control and lenalidomide-treated CARTs (n = 3 independent experiments with distinct donors). Statistical significance was determined using two-tailed ratio paired t-test (**d** and **h**).

Reporting Summary

Nature Portfolio wishes to improve the reproducibility of the work that we publish. This form provides structure for consistency and transparency in reporting. For further information on Nature Portfolio policies, see our [Editorial Policies](#) and the [Editorial Policy Checklist](#).

Statistics

For all statistical analyses, confirm that the following items are present in the figure legend, table legend, main text, or Methods section.

- | n/a | Confirmed |
|-------------------------------------|------------------------------------------------------------------------------------------------------------------------------------------------------------------------------------------------------------------------------------------------------------------------------------------------|
| <input type="checkbox"/> | <input checked="" type="checkbox"/> The exact sample size (n) for each experimental group/condition, given as a discrete number and unit of measurement |
| <input type="checkbox"/> | <input checked="" type="checkbox"/> A statement on whether measurements were taken from distinct samples or whether the same sample was measured repeatedly |
| <input type="checkbox"/> | <input checked="" type="checkbox"/> The statistical test(s) used AND whether they are one- or two-sided
<i>Only common tests should be described solely by name; describe more complex techniques in the Methods section.</i> |
| <input checked="" type="checkbox"/> | <input type="checkbox"/> A description of all covariates tested |
| <input type="checkbox"/> | <input checked="" type="checkbox"/> A description of any assumptions or corrections, such as tests of normality and adjustment for multiple comparisons |
| <input type="checkbox"/> | <input checked="" type="checkbox"/> A full description of the statistical parameters including central tendency (e.g. means) or other basic estimates (e.g. regression coefficient) AND variation (e.g. standard deviation) or associated estimates of uncertainty (e.g. confidence intervals) |
| <input type="checkbox"/> | <input checked="" type="checkbox"/> For null hypothesis testing, the test statistic (e.g. F , t , r) with confidence intervals, effect sizes, degrees of freedom and P value noted
<i>Give P values as exact values whenever suitable.</i> |
| <input checked="" type="checkbox"/> | <input type="checkbox"/> For Bayesian analysis, information on the choice of priors and Markov chain Monte Carlo settings |
| <input checked="" type="checkbox"/> | <input type="checkbox"/> For hierarchical and complex designs, identification of the appropriate level for tests and full reporting of outcomes |
| <input checked="" type="checkbox"/> | <input type="checkbox"/> Estimates of effect sizes (e.g. Cohen's d , Pearson's r), indicating how they were calculated |

Our web collection on [statistics for biologists](#) contains articles on many of the points above.

Software and code

Policy information about [availability of computer code](#)

Data collection BD FACSDiva software v8.0.1(LSRII, Fortessa, A3 Lite, and ArialI) for flow cytometry data. Gen5 3.04 for in vitro killing assay data. Living Image 4.4 (PerkinElmer) for bioluminescence flux data. Zen 2.5 (blue edition, Zeiss) software for microscopy data.

Data analysis FlowJo v10.8.1 for flow cytometry data. Living Image 4.4 (PerkinElmer) for bioluminescence flux data. Statistical analyses were performed using GraphPad Prism (v9.4.0).
 For single cell analysis, fastq files were analyzed with Cell Ranger v6.1.2.
 No custom code was created for this study.
 The code used was deposited to Zenodo (10.5281/zenodo.11672288).

For analysis performed in R, we used the following packages:
 #R version 4.3.1 (2023-06-16)
 #Platform: aarch64-apple-darwin20 (64-bit)
 #Running under: macOS Monterey 12.6.2
 #Matrix products: default
 #BLAS: /System/Library/Frameworks/Accelerate.framework/Versions/A/Frameworks/vecLib.framework/Versions/A/libBLAS.dylib
 #LAPACK: /Library/Frameworks/R.framework/Versions/4.3-arm64/Resources/lib/libRlapack.dylib; LAPACK version 3.11.0
 #locale:
 # [1] en_US.UTF-8/en_US.UTF-8/en_US.UTF-8/C/en_US.UTF-8/en_US.UTF-8
 #time zone: America/New_York
 #tzcode source: internal

```

#attached base packages:
# [1] stats4 grid stats graphics grDevices utils datasets methods base

#other attached packages:
# [1] ggplot2_3.5.1 RColorBrewer_1.1-3 DropletUtils_1.20.0
# [4] SingleCellExperiment_1.24.0 SummarizedExperiment_1.32.0 Biobase_2.62.0
# [7] GenomicRanges_1.54.1 GenomeInfoDb_1.38.5 IRanges_2.36.0
# [10] S4Vectors_0.40.2 BiocGenerics_0.48.1 MatrixGenerics_1.14.0
# [13] matrixStats_1.3.0 glmGamPoi_1.14.0 gridExtra_2.3
# [16] EnhancedVolcano_1.18.0 ggrepel_0.9.5 sctransform_0.4.1
# [19] dplyr_1.1.4 cowplot_1.1.3 fgsea_1.26.0
# [22] patchwork_1.2.0 ggplot2_3.5.1 SeuratObject_5.0.2
# [25] Seurat_4.4.0 rlang_1.1.3 irlba_2.3.5.1
# [28] Matrix_1.6-5

#loaded via a namespace (and not attached):
# [1] RcppAnnoy_0.0.22 splines_4.3.1 later_1.3.2
# [4] bitops_1.0-7 R.oo_1.26.0 tibble_3.2.1
# [7] polyclip_1.10-6 lifecycle_1.0.4 edgeR_3.42.4
# [10] globals_0.16.3 lattice_0.22-6 MASS_7.3-60.0.1
# [13] magrittr_2.0.3 limma_3.56.2 plotly_4.10.4
# [16] remotes_2.5.0 httpuv_1.6.15 spam_2.10-0
# [19] sp_2.1-4 sessioninfo_1.2.2 pkgbuild_1.4.4
# [22] spatstat.sparse_3.0-3 reticulate_1.37.0 pbapply_1.7-2
# [25] abind_1.4-5 pkgload_1.3.4 zlibbioc_1.48.0
# [28] Rtsne_0.17 purrr_1.0.2 R.utils_2.12.3
# [31] RCurl_1.98-1.14 GenomeInfoDbData_1.2.11 listenv_0.9.1
# [34] spatstat.utils_3.0-4.001 goftest_1.2-3 dqrng_0.4.1
# [37] spatstat.random_3.2-3 fitdistrplus_1.1-11 parallelly_1.37.1
# [40] DelayedMatrixStats_1.24.0 leiden_0.4.3.1 codetools_0.2-19
# [43] DelayedArray_0.28.0 scuttle_1.10.3 tidyselect_1.2.1
# [46] farver_2.1.2 spatstat.explore_3.2-7 jsonlite_1.8.8
# [49] ellipsis_0.3.2 progressr_0.14.0 ggridges_0.5.6
# [52] survival_3.5-8 tools_4.3.1 ica_1.0-3
# [55] Rcpp_1.0.12 glue_1.7.0 SparseArray_1.2.3
# [58] usethis_2.2.3 HDF5Array_1.30.0 withr_3.0.0
# [61] fastmap_1.2.0 rhdf5filters_1.14.1 fansi_1.0.6
# [64] digest_0.6.35 R6_2.5.1 mime_0.12
# [67] colorspace_2.1-0 scattermore_1.2 tensor_1.5
# [70] spatstat.data_3.0-4 R.methodsS3_1.8.2 utf8_1.2.4
# [73] tidyr_1.3.1 generics_0.1.3 data.table_1.15.4
# [76] httr_1.4.7 htmlwidgets_1.6.4 S4Arrays_1.2.0
# [79] uwot_0.2.2 pkgconfig_2.0.3 gtable_0.3.5
# [82] lmtest_0.9-40 XVector_0.42.0 htmltools_0.5.8.1
# [85] profvis_0.3.8 dotCall64_1.1-1 scales_1.3.0
# [88] png_0.1-8 rstudioapi_0.15.0 reshape2_1.4.4
# [91] nlme_3.1-164 cachem_1.1.0 zoo_1.8-12
# [94] rhdf5_2.46.0 stringr_1.5.1 KernSmooth_2.23-22
# [97] parallel_4.3.1 miniUI_0.1.1.1 pillar_1.9.0
# [100] vctrs_0.6.5 RANN_2.6.1 urlchecker_1.0.1
# [103] promises_1.3.0 beachmat_2.18.0 xtable_1.8-4
# [106] cluster_2.1.6 locfit_1.5-9.9 cli_3.6.2
# [109] compiler_4.3.1 crayon_1.5.2 future.apply_1.11.2
# [112] labeling_0.4.3 plyr_1.8.9 fs_1.6.4
# [115] stringi_1.8.4 viridisLite_0.4.2 deldir_2.0-4
# [118] BiocParallel_1.36.0 munsell_0.5.1 lazyeval_0.2.2
# [121] devtools_2.4.5 spatstat.geom_3.2-9 sparseMatrixStats_1.14.0
# [124] future_1.33.2 Rhdf5lib_1.24.0 shiny_1.8.1.1
# [127] ROCR_1.0-11 igraph_2.0.3 memoise_2.0.1
# [130] fastmatch_1.1-4

```

For code used in python (pyscenic analysis), we used the following packages:

```

-----
anndata 0.8.0
scanpy 1.7.2
sinfo 0.3.1
-----
MulticoreTSNE NA
PIL 9.1.0
anndata 0.8.0
anyio NA
appnope 0.1.3
arrow 1.2.3
attr 21.4.0
babel 2.14.0
backcall 0.2.0

```

```

beta_ufunc      NA
binom_ufunc    NA
bottleneck     1.3.4
brotli         NA
cached_property 1.5.2
certifi        2021.10.08
cffi           1.15.0
charset_normalizer 2.0.12
cloudpickle    2.0.0
colorama       0.4.4
cyclor         0.10.0
cython_runtime NA
cytoolz        0.11.0
dask           2022.02.0
dateutil       2.8.2
debugpy        1.6.0
decorator      5.1.1
defusedxml     0.7.1
dunamai        1.11.1
entrypoints    0.4
fastjsonschema NA
fqdn           NA
fsspec         2022.3.0
get_version    3.5.4
h5py           3.6.0
idna           3.3
igraph         0.9.10
importlib_resources NA
ipykernel      6.16.2
ipython_genutils 0.2.0
isoduration    NA
jedi           0.18.1
jinja2         3.1.1
joblib         1.1.0
json5          NA
jsonpointer    2.4
jsonschema     4.17.3
jupyter_server 1.24.0
jupyterlab_server 2.24.0
kiwisolver     1.4.2
legacy_api_wrap 0.0.0
llvmlite       0.38.0
loompy         3.0.7
louvain        0.7.1
markupsafe     2.1.1
matplotlib     3.5.1
matplotlib_inline NA
mpl_toolkits   NA
natsort        8.1.0
nbformat       5.3.0
nbinom_ufunc   NA
numba          0.55.1
numexpr        2.8.0
numpy          1.21.6
numpy_groupies 0.9.14
packaging      21.3
pandas         1.3.4
parso          0.8.3
pexpect        4.8.0
pickleshare    0.7.5
pkg_resources  NA
prometheus_client NA
prompt_toolkit 3.0.39
psutil         5.9.0
ptyprocess     0.7.0
pvectorc       NA
pyarrow        0.16.0
pyparser       2.21
pydev_ipython  NA
pydevconsole   NA
pydevd         2.8.0
pydevd_file_utils NA
pydevd_plugins NA
pydevd_tracing NA
pygments       2.11.2
pyparsing      3.0.8

```



```

pyrsistent      NA
pyscenic        0.11.2
pytz            2022.1
requests        2.31.0
rfc3339_validator 0.1.4
rfc3986_validator 0.1.1
scanpy          1.7.2
scipy           1.7.3
send2trash      NA
setuptools      62.1.0
setuptools_scm  NA
sinfo           0.3.1
six             1.16.0
sklearn         1.0.2
sniffio         1.3.1
socks           1.7.1
sphinxcontrib   NA
storemagic      NA
tables          3.7.0
tblib           1.7.0
terminado       0.13.3
texttable       1.6.4
threadpoolctl   3.1.0
tlz             0.11.0
toolz           0.11.1
tornado         6.1
traitlets       5.9.0
typing_extensions NA
unicodedata2    NA
uri_template    NA
urllib3         1.26.9
wcwidth         0.2.5
webcolors       1.13
websocket       1.6.1
yaml            6.0
zipp            NA
zmq             22.3.0
-----
IPython         7.32.0
jupyter_client  7.2.2
jupyter_core    4.12.0
jupyterlab      3.6.7
notebook        6.4.10
-----
Python 3.7.12 | packaged by conda-forge | (default, Oct 26 2021, 05:59:23) [Clang 11.1.0 ]
Darwin-21.6.0-x86_64-i386-64bit
10 logical CPU cores, i386

For python analysis of RNA velocity, the following packages were used:
-----
anndata 0.8.0
scanpy 1.8.2
sinfo 0.3.1
-----
PIL 9.0.1
anndata 0.8.0
appnope 0.1.2
asttokens NA
backcall 0.2.0
beta_ufunc NA
binom_ufunc NA
cellrank 1.5.1
cffi 1.15.0
colorama 0.4.4
cyclcr 0.10.0
cython_runtime NA
dateutil 2.8.2
debugpy 1.5.1
decorator 5.1.1
defusedxml 0.7.1
docrep 0.3.2
entrypoints 0.4
executing 0.8.3
h5py 3.6.0
hypergeom_ufunc NA
igraph 0.10.0

```

```

ipykernel          6.9.2
ipython_genutils  0.2.0
jedi               0.18.1
joblib            1.1.0
kiwisolver        1.4.0
llvmlite          0.38.0
louvain           0.7.1
matplotlib        3.5.1
matplotlib_inline NA
mpl_toolkits      NA
natsort           8.1.0
nbinom_ufunc      NA
numba             0.55.1
numexpr           2.8.0
numpy             1.21.5
packaging         21.3
pandas            1.4.1
parso             0.8.3
petsc4py          3.16.5
pexpect           4.8.0
pickleshare       0.7.5
pkg_resources     NA
progressbar       4.0.0
prompt_toolkit    3.0.27
psutil            5.9.0
ptyprocess        0.7.0
pure_eval         0.2.2
pydev_ipython     NA
pydevconsole      NA
pydevd            2.6.0
pydevd_concurrency_analyser NA
pydevd_file_utils NA
pydevd_plugins    NA
pydevd_tracing    NA
pygam             0.8.0
pygments          2.11.2
pygpcca           1.0.3
pyparsing         3.0.7
python_utils      NA
pytz              2022.1
scanpy            1.8.2
scipy             1.8.0
scvelo            0.2.4
seaborn           0.11.2
setuptools        60.10.0
sinfo             0.3.1
six               1.16.0
sklearn           1.0.2
slepc4py          3.16.1
sphinxcontrib     NA
stack_data        0.2.0
statsmodels       0.13.2
tables            3.7.0
texttable         1.6.4
threadpoolctl     3.1.0
tornado           6.1
tqdm              4.63.1
traitlets         5.1.1
typing_extensions NA
wcwidth           0.2.5
wrap              1.14.0
zipp              NA
zmq               22.3.0
-----
IPython           8.1.1
jupyter_client    7.1.2
jupyter_core      4.9.2
notebook          6.4.10
-----
Python 3.10.4 | packaged by conda-forge | (main, Mar 24 2022, 17:45:10) [Clang 12.0.1 ]
macOS-12.6.2-x86_64-i386-64bit
10 logical CPU cores, i386

```

For manuscripts utilizing custom algorithms or software that are central to the research but not yet described in published literature, software must be made available to editors and reviewers. We strongly encourage code deposition in a community repository (e.g. GitHub). See the Nature Portfolio [guidelines for submitting code & software](#) for further information.

Data

Policy information about [availability of data](#)

All manuscripts must include a [data availability statement](#). This statement should provide the following information, where applicable:

- Accession codes, unique identifiers, or web links for publicly available datasets
- A description of any restrictions on data availability
- For clinical datasets or third party data, please ensure that the statement adheres to our [policy](#)

Sequencing data have been deposited on GEO with accession number GSE268878. The reference genome for single cell RNA sequencing analysis is Human (GRCh38) 2020-A, Human (GRCh38) v5.0.0.

Human research participants

Policy information about [studies involving human research participants and Sex and Gender in Research](#).

Reporting on sex and gender	Healthy human donors of male and female sexes were used in this study. Sex was determined by self reporting information collected by the Penn Human Immunology Core. Study was not designed to detect differences between sexes.
Population characteristics	T cells were isolated from healthy human donors by the Penn Human Immunology Core.
Recruitment	Apheresis product was collected from healthy human donors by the Penn Human Immunology Core. Samples were used without any selection
Ethics oversight	All human studies were in compliance with the Declaration of Helsinki. Apheresis donors were recruited by the Penn Human Immunology Core, which maintains the IRB protocols at the University of Pennsylvania necessary for human cell procurement and distribution of de-identified reagents.

Note that full information on the approval of the study protocol must also be provided in the manuscript.

Field-specific reporting

Please select the one below that is the best fit for your research. If you are not sure, read the appropriate sections before making your selection.

Life sciences Behavioural & social sciences Ecological, evolutionary & environmental sciences

For a reference copy of the document with all sections, see [nature.com/documents/nr-reporting-summary-flat.pdf](https://www.nature.com/documents/nr-reporting-summary-flat.pdf)

Life sciences study design

All studies must disclose on these points even when the disclosure is negative.

Sample size	Sample sizes were not predetermined based on statistical methods, but were chosen based on preliminary data and previously published results. We performed at least three independent experiments for flow cytometry, in vitro cytotoxicity, and real-time metabolic assay experiments; 5-8 NSG mice per treatment group; and 2 independent single-cell profiling experiments. Sample size is stated in each caption.
Data exclusions	Negative OCR values in the real-time metabolic assay was set to zero, as negative values do not represent biological meaning and are appreciated to be technical artifacts when studying 1.5×10^5 T cells per well. Bioluminescence outliers were removed from plotting but included in source data.
Replication	Reported results were replicated across multiple experiments with all replicates generating consistent results. The number of replicates for each experiment are detailed in the figure legends.
Randomization	For all in vivo experiments, treatment groups were randomly selected by the cage number. Randomization was not required for in vitro experiments as each experimental condition was controlled within each T cell donor (e.g. proximal and distal daughter cells from the same donor).
Blinding	In vivo injections were performed in a blinded fashion by a member of the Ellebrecht or Payne laboratories or a staff member of the Human Stem Cell and Xenograft Core of the University of Pennsylvania. For all in vitro experiments, data collection was not blinded, however, data were obtained with objective methodologies (sequencing, flow cytometry). Fully blinded in vitro experiments were not possible due to limited staff availability.

Reporting for specific materials, systems and methods

We require information from authors about some types of materials, experimental systems and methods used in many studies. Here, indicate whether each material, system or method listed is relevant to your study. If you are not sure if a list item applies to your research, read the appropriate section before selecting a response.

Materials & experimental systems

- | | | |
|-------------------------------------|-------------------------------------|-------------------------------|
| n/a | <input type="checkbox"/> | Involved in the study |
| <input type="checkbox"/> | <input checked="" type="checkbox"/> | Antibodies |
| <input type="checkbox"/> | <input checked="" type="checkbox"/> | Eukaryotic cell lines |
| <input checked="" type="checkbox"/> | <input type="checkbox"/> | Palaeontology and archaeology |
| <input type="checkbox"/> | <input checked="" type="checkbox"/> | Animals and other organisms |
| <input checked="" type="checkbox"/> | <input type="checkbox"/> | Clinical data |
| <input checked="" type="checkbox"/> | <input type="checkbox"/> | Dual use research of concern |

Methods

- | | | |
|-------------------------------------|-------------------------------------|------------------------|
| n/a | <input type="checkbox"/> | Involved in the study |
| <input checked="" type="checkbox"/> | <input type="checkbox"/> | ChIP-seq |
| <input type="checkbox"/> | <input checked="" type="checkbox"/> | Flow cytometry |
| <input checked="" type="checkbox"/> | <input type="checkbox"/> | MRI-based neuroimaging |

Antibodies

Antibodies used

Unless otherwise specified, antibodies were purchased from BioLegend.

LIPSTIC assay populations were sorted and subsequently phenotyped by staining with CD8-APCH7 (SK1, BD Biosciences, 561423), CD4-BUV805 (SK3, BD Biosciences, 612887), CCR7-APC/Cy7 (G043H7, 353212), CD45RA-BV650 (HI100, 304136), CD45RA-BUV395 (HI100, BD Biosciences, 740298), CD45RO (UCHL1, 304234), CD25-BV711 (M-A251, 356138), CD62L-PE (DREG-56, 304840), and/or CD62L-BV605 (DREG-56, 304834).

For in vivo studies, samples were stained with CD8-APC/Cy5.5 (RFT8, SouthernBiotech 9536-18), CD4-PE/Cy5.5 (RFT4, SouthernBiotech 9522-16), CD3-BV605 (OKT3, 317322), CD19-APC (HIB19, 302212), CD45RA-BUV395 (HI100, 740298), CD45RO-BV785 (UCHL1, 304234), and CD45-PECy7 (QA17A19, 393408).

The following antibodies were used for western blots: rabbit anti-Ikaros (IKZF1) monoclonal antibody (Cell Signaling, 90345), digital anti-rabbit-HRP (Kindle Biosciences, LLC, R1006), mouse anti- β -actin monoclonal antibody (Cell Signaling, 37005), and digital anti-mouse-HRP (Kindle Biosciences, LLC, R1005).

The pre-mixed totalseq C human super panel cocktail by Biolegend was used (cat# 900000114, lot# B311489). The dilution and concentration of each antibody in this cocktail is proprietary information owned by Biolegend and not available to us. The following clones are included in the panel (along with their DNA barcode):

The order of the following lines is as follows: id of antibody - Clone name - target specificity - DNA sequence

C0005 2D10 CD80 ACGAATCAATCTGTG
 C0006 IT2.2 CD86 GTCITTTGTCAAGTGCA
 C0007 29E.2A3 CD274B7-H1PD-L1 GTTGTCGACAATAC
 C0008 24F.10C12 CD273B7-DCPD-L2 TCAACGCTTGGCTAG
 C0009 2D3 CD275B7-H2ICOSL GTGCATTCAACAGTA
 C0020 122 CD270HVEMTR2 TGATAGAAACAGACC
 C0021 11C3.1 CD252OX40L TTTAGTGATCCGACT
 C0022 5F4 CD137L4-1BBLigand ATTCGCCTTACGCAA
 C0023 SKII.4 CD155PVR ATCACATCGTTGCCA
 C0024 TX31 CD112Nectin-2 AACCTCCGTCTAAG
 C0026 CC2C6 CD47 GCATTCTGTCACTA
 C0027 113-16 CD70 CGCGAACATAAGAAG
 C0028 BY88 CD30 TCAGGGTGTGCTGTA
 C0029 BJ40 CD48 CTACGACGTAGAAGA
 C0031 5C3 CD40 CTAGATGGAGTATG
 C0032 24-31 CD154 GCTAGATAGATGCAA
 C0033 HI186 CD52 CTTTGTACGAGCAA
 C0034 UCHT1 CD3 CTATTGTAACCTCT
 C0046 SK1 CD8 GCGCAACTTGATGAT
 C0047 5.1H11 CD56 TCCTTTCCTGATAGG
 C0050 HIB19 CD19 CTGGGCAATTACTCG
 C0052 P67.6 CD33 TAACTCAGGGCCTAT
 C0053 S-HCL-3 CD11c TACGCCTATAACTTG
 C0054 581 CD34 GCAGAAATCTCCCTT
 C0056 19F2 CD269BCMA CAGATGATCCACCAT
 C0058 W6/32 HLA-ABC TATGCGAGGCTTATC
 C0061 104D2 CD117c-kit AGACTAATAGCTGAC
 C0062 HI10a CD10 CAGCCATTCATTAGG
 C0063 HI100 CD45RA TCAATCCTCCGCTT
 C0064 6H6 CD123 TTCACTCTGTCAAGG
 C0066 CD7-6B7 CD7 TGGATTCGCGGACTT
 C0068 43A3 CD105 ATCGTCGAGAGCTAG
 C0069 RCR-401 CD201EPCR GTTTCCTTGACCAAG
 C0070 GoH3 mouseCD49f TTCCGAGGATGATCT
 C0071 L291H4 CD194CCR4 AGCTTACCTGCACGA
 C0072 RPA-T4 CD4 TGTTCCCGCTCAACT
 C0073 IM7 CD44 TGGCTTCAGGTCCTA
 C0081 M5E2 CD14 TCTCAGACCTCCGTA
 C0083 3G8 CD16 AAGTTCACCTTTTGC
 C0085 BC96 CD25 TTTGTCCTGTACGCC
 C0087 UCHL1 CD45RO CTCCGAATCATGTTG

C0088 EH12.2H7 CD279 ACAGCGCCGTATTTA
C0089 A15153G TIGITVSTM3 TTGCTTACCGCCAGA
C0090 MOPC-21 MouseIlgG1kappaisotypeCtrl GCCGGACGACATTAA
C0091 MOPC-173 MouseIlgG2akappaisotypeCtrl CTCCTACCTAAACTG
C0092 H1.2F3 MouseIlgG2bkappaisotypeCtrl ATATGTATCACGCGA
C0095 RTK4530 RatIlgG2bkappaisotypeCtrl GATTCTTGACGACCT
C0100 2H7 CD20 TTCTGGGTCCCTAGA
C0101 900 CD335NKp46 ACAATTTGAACAGCG
C0102 BM16 CD294CRTH2 TGTTTACGAGAGCCG
C0103 RA3-6B2 CD45R/B220 CCTACACCTCATAAT
C0123 9C4 CD326Ep-CAM TTCCGAGCAAGTATC
C0124 WM59 CD31 ACCTTTATGCCACGG
C0127 NC-08 Podoplanin GGTACTCGTTGTGT
C0128 16A1 CD140aPDGFRalpha ATGCGCCGAGAATTA
C0129 18A2 CD140bPDGFRbeta CAATGGTTCACTGCC
C0132 AY13 EGFR GCTTAACATTGGCAC
C0134 P1H12 CD146 CCTTGGATAACATCA
C0135 67A4 CD324E-Cadherin ATCCTTCTCCCTTTC
C0136 MHM-88 IgM TAGCGAGCCCGTATA
C0138 UCHT2 CD5 CATTAAACGGGATGCC
C0139 B1 TCRdeltagamma CTTCCGATTCAATCA
C0140 G025H7 CD183CXCR3 GCGATGGTAGATTAT
C0141 J418F1 CD195CCR5 CCAAAGTAAGAGCCA
C0142 FUN-2 CD32 GCTTCCGAATTACCG
C0143 G034E3 CD196CCR6 GATCCCTTTGTCACT
C0144 J252D4 CD185CXCR5 AATTCAACCGTCGCC
C0145 Ber-ACT8 CD103IntegrinalphaE GACCTCATTGTGAAT
C0146 FN50 CD69 GTCTCTTGGCTTAAA
C0147 DREG-56 CD62L GTCCTGCAACTTGA
C0148 G043H7 CD197CCR7 AGTTCAGTCAACCGA
C0149 HP-3G10 CD161 GTACGCAGTCCTTCT
C0151 BNI3 CD152CTLA-4 ATGGTTCACGTAATC
C0152 11C3C65 CD223LAG-3 CATTGTCTGCCGGT
C0153 SA231A2 KLRG1MAFA CTTATTTCTGCCCT
C0154 O323 CD27 GCACTCCTGCATGTA
C0155 H4A3 CD107aLAMP-1 CAGCCCACTGCAATA
C0156 DX2 CD95Fas CCAGCTCATTAGAGC
C0158 Ber-ACT35 (ACT35) CD134OX40 AACCCACCGTTGTTA
C0159 L243 HLA-DR AATAGCGAGCAAGTA
C0160 L161 CD1c GAGTACTTCACTCG
C0161 ICRF44 CD11b GACAAGTGATCTGCA
C0162 10.1 CD64 AAGTATGCCCTACGA
C0163 M80 CD141Thrombomodulin GGATAACCGCGCTTT
C0164 51.1 CD1d TCGAGTCGCTTATCA
C0165 1D11 CD314NKG2D CGTGTGTTGTTCTCA
C0166 6/40c CD66b AGCTGTAAGTTTCGG
C0167 E11 CD35 ACTTCCGTCGATCTT
C0168 QA17A04 CD57Recombinant AACTCCCTATGGAGG
C0169 F38-2E2 CD366Tim-3 TGTCTACCCAATT
C0170 MIH26 CD272BTLA GTTATTGGACTAAGG
C0171 C398.4A CD278ICOS CGCGCACCCATTA
C0174 TS2/9 CD58LFA-3 GTTCCTATGGACGAC
C0175 NK92.39 CD96TACTILE TGGCCTATAAATGGT
C0176 A1 CD39 TTACCTGGTATCCGT
C0177 NOK-1 CD178Fas-L CCGGTCCTCTGTATT
C0179 K0124E1 CX3CR1 AGTATCGTCTCTGGG
C0180 ML5 CD24 AGATTCCTTCGTGTT
C0181 Bu32 CD21 AACCTAGTAGTTCCGG
C0185 TS2/4 CD11a TATATCCTTGTGAGC
C0187 CB3-1 CD79bigB ATTCTTCAACCGAAG
C0188 ASL-32 CD66ace GGGACAGTTCTTTC
C0189 C1.7 CD2442B4 TCGCTTGGATGGTAG
C0196 HIR2 CD235ab GCTCCTTACACGTA
C0205 15-2 CD206MMR TCAGAAGTCTAACT
C0206 7-239 CD169SialoadhesinSiglec-1 TACTCAGCGTGTGTTG
C0207 8F9 CD370CLEC9ADNGR1 CTGCATTTCAAGTAAG
C0208 S15046E XCR1 AAGACGCATGTCAAC
C0213 MHN1-519 Notch1 AATCTGTAGTGCCTT
C0214 FIB504 integrinbeta7 TCCTTGGATGTACCG
C0215 11C1 CD268BAFF-R CGAAGTCGATCCGTA
C0216 HIP1 CD42b TCCTAGTACCGAAGT
C0217 HA58 CD54 CTGATAGACTTGAGT
C0218 AK4 CD62PP-Selectin CCTTCCGTATCCCTT
C0219 GIR-208 CD119IFNgammaRalphachain TGTGTATTCCCTTGT
C0224 IP26 TCRalpha/beta CGTAACGTAGAGCGA
C0233 MHN3-21 Notch3 CTATTGGACGTATCT

C0236 RTK2071 RatlgG1kappaisotypeCtrl ATCAGATGCCCTCAT
C0238 RTK2758 RatlgG2akappaisotypeCtrl AAGTCAGGTTCTGTTT
C0241 HTK888 ArmenianHamsterIlgIsotypeCtrl CCTGTCATTAAGACT
C0245 STA CD106 TCACAGTTCCTTGGA
C0246 TU27 CD122IL-2Rbeta TCATTTCTCCGATT
C0247 1A1 CD267TACI AGTGATGGAGCGAAC
C0248 HAE-1f CD62E CTCCTGTGGCTTAA
C0352 AER-37 (CRA-1) FcepsilonRIalpha CTCGTTTCCGTATCG
C0353 HIP8 CD41 ACGTTGTGGCCTTGT
C0355 4B4-1 CD1374-1BB CAGTAAGTTCGGGAC
C0356 MIH24 CD254TRANCERANKL TCCGTGTTAGTTTGT
C0358 GHI/61 CD163 GCTTCTCCTTCTTA
C0359 HB15e CD83 CCACTCATTTCCGGT
C0360 108-17 CD357GITR ACCTTTCGACACTCG
C0363 G077F6 CD124IL-4Ralpha CCGTCTGATAGATG
C0364 WM15 CD13 TTTCAACGCCCTTTC
C0366 12G5 CD184CXCR4 TCAGGTCTTTCAAC
C0367 TS1/8 CD2 TACGATTTGTACGGG
C0368 11A8 CD226DNAM-1 TCTCAGTGTTTGTGG
C0369 TS2/16 CD29 GTATTCCTCAGTCA
C0370 201A CD303BDCA2 GAGATGTCCGAATTT
C0371 P1E6-C5 CD49b GCTTTCTCAGTATG
C0373 5A6 CD81TAPA-1 GTATCCTTCTTGGC
C0374 MEM-108 CD98 GCACCAACAGCCATT
C0375 M1310G05 IgGFc CTGGAGCGATTAGAA
C0384 IA6-2 IgD CAGTCTCCGTAGAGT
C0385 TS1/18 CD18 TATTGGGACACTTCT
C0386 CD28.2 CD28 TGAGAACGACCCTAA
C0387 1D3 TSLPRTSLP-R CAGTCCTCTCTGTCA
C0389 HIT2 CD38 TGTACCCGCTTGTGA
C0390 A019D5 CD127IL-7R GTGTGTTGCCTATG
C0391 HI30 CD45 TGCAATTACCCGGAT
C0393 S-HCL-1 CD22 GGGTTGTTGTCTTTG
C0394 CY1G4 CD71 CCGTGTTCTCCTTA
C0395 MIH43 B7-H4 TGTATGTCTGCCTTG
C0396 BA5b CD26 GGTGGCTAGATAATG
C0399 7C9C20 CD204 TAGCGAGCCAGATGT
C0400 BV9 CD144VE-Cadherin TCCACTCATTCTGTA
C0402 HI149 CD1a GATCGTGTGTGTTA
C0406 12C2 CD304Neuropilin-1 GGACTAAGTTTCGTT
C0407 5-271 CD36 TTCTTTGCCTTGCCA
C0420 HP-MA4 CD158KIR2DL1S1S3S5 TATCAACCAACGCTT
C0433 8C11 CD325N-Cadherin CCTTCCCTTTCCTCT
C0437 4C7 aCD207 CGATTTGTATCCCT
C0575 TS2/7 CD49a ACTGATGGACTCAGA
C0576 9F10 CD49d CCATTCAACTCCGG
C0577 AD2 CD73 CAGTTCCTCAGTTCG
C0581 3C10 TCRValpha72 TACGAGCAGTATTCA
C0582 B6 TCRVdelta2 TCAGTCAGATGGTAT
C0583 B3 TCRVgamma9 AAGTGATGGTATCTG
C0584 6B11 TCRValpha24 AACTTCTGTGGTAGC
C0590 NKTA255 CD305LAIR1 ATTTCCATTCCCTGT
C0591 15C4 LOX-1 ACCCTTTACCGAATA
C0592 DX27 CD158bKIR2DL2L3NKAT2 GACCCGTAGTTTGTAT
C0597 9E9A8 CD209DC-SIGN TCACTGGACACTTAA
C0599 DX9 CD158e1KIR3DL1NKB1 GGACGCTTTCCTTGA
C0600 UP-R1 CD158fKIR2DL5 AAAGTGATGCCACTG
C0801 P30-15 CD337NKp30 AAAGTCACTCTGCCG
C0802 P44-8 CD336NKp44 GGGCAATTAGCGAGT
C0828 413D12 CD307dFcRL4 CGATTTGATCTGCCT
C0829 509f6 CD307eFcRL5 TCACGCAGTCCTCAA
C0830 162.1 CD319CRACC AGTATGCCATGTCTT
C0845 3B2/TA8 CD99 ACCCGTCCCTAAGAA
C0853 50C1 CLEC12A CATTAGAGTCTGCCA
C0863 1D6 CD257BAFFBLYS CAGAGCACCCATTAA
C0864 NT-7 CD352NTB-A AGTTTCCACTCAGGC
C0867 DX22 CD94 CTTTCCGGTCTTACA
C0870 A12 (7D4) CD150SLAM GTCATTGTATGTCTG
C0894 MHK-49 Iglighchainkappa AGCTCAGCCAGTATG
C0895 M3/38 Mac-2 GATGCAATTAGCCGG
C0896 GHI/75 CD85jILT2 CCTTGTGAGGCTATG
C0897 EBVCS-5 CD23 TCTGTATAACCGTCT
C0898 MHL-38 Iglighchainlambda CAGCCAGTAAGTCAC
C0899 BB7.2 HLAA2 GAACATTTCCGACAA
C0901 7B11 GARPLRRC32 AGGTATGGTAGAGTA
C0902 6-434 CD328Siglec-7 CTTAGCATTTCACTG

C0908 H131 TCRVbeta131 TTATGGACGTATGGT
 C0912 CG4 GPR56 GCCTAGTTCCGTTT
 C0918 3D12 HLA-E GAGTCGAGAAATCAT
 C0920 ASL-24 CD82 TCCCCTCCGCTTT
 C0944 BB27 CD101BB27 CTACTTCCCTGTCAA
 C0985 17A12 CD360IL-21R GAGGATGATGCCATG
 C1046 S5/1 CD88C5aR GCCGCATGAGAAACA
 C1051 mAb 84 Podocalyxin GAGCCGGTATAATGC
 C1052 KF29 CD224 CTGATGAGATGTCAG
 C1056 T5-39 CD258LIGHT ACTTCCCTGTAGAAA
 C1057 JD3 DR3TRAMP GAGTCCCTCAGTTC
 C0956 APC-Streptavidin APC-Streptavidin GGTAActCTGGTAGC

Validation

Unless specified otherwise, antibodies were purchased from Biolegend.

CD8-APCH7 (SK1, BD Biosciences, 561423): <https://www.bdbiosciences.com/en-us/products/reagents/flow-cytometry-reagents/research-reagents/single-color-antibodies-ruo/apc-h7-mouse-anti-human-cd8.561423>
 CD4-BUV805 (SK3, BD Biosciences, 612887): <https://www.bdbiosciences.com/en-us/products/reagents/flow-cytometry-reagents/research-reagents/single-color-antibodies-ruo/buv805-mouse-anti-human-cd4.612887>
 CD45RA-BUV395 (HI100, BD Biosciences, 740298): <https://www.bdbiosciences.com/en-us/products/reagents/flow-cytometry-reagents/research-reagents/single-color-antibodies-ruo/buv395-mouse-anti-human-cd45ra.740298>
 CD45RO (UCHL1, 304234): <https://www.biolegend.com/en-us/products/brilliant-violet-785-anti-human-cd45ro-antibody-7973>
 CD25-BV711 (M-A251, 356138): <https://www.biolegend.com/en-us/products/brilliant-violet-711-anti-human-cd25-antibody-13762>
 CD62L-PE (DREG-56, 304840): <https://www.biolegend.com/en-us/products/pe-anti-human-cd62l-antibody-653?GroupID=BLG10034>
 CD8-APC/Cy5.5 (RFT8, SouthernBiotech 9536-18): <https://www.southernbiotech.com/mouse-anti-human-cd8-apc-cy5-5-rft8-9536-18>
 CD4-PE/Cy5.5 (RFT4, SouthernBiotech 9522-16): <https://www.southernbiotech.com/mouse-anti-human-cd4-pe-cy5-5-rft4-9522-16>
 CD3-BV605 (OKT3, 317322): <https://www.biolegend.com/en-us/products/brilliant-violet-605-anti-human-cd3-antibody-7666>
 CD19-APC (HIB19, 302212): <https://www.biolegend.com/en-us/products/apc-anti-human-cd19-antibody-715>
 CD45RA-BUV395 (HI100, BD Biosciences, 740298): <https://www.bdbiosciences.com/en-us/products/reagents/flow-cytometry-reagents/research-reagents/single-color-antibodies-ruo/buv395-mouse-anti-human-cd45ra.740298>
 CD45RO-BV785 (UCHL1, 304234): <https://www.biolegend.com/en-us/products/brilliant-violet-785-anti-human-cd45ro-antibody-7973?GroupID=GROUP658>
 CD45-PECy7 (QA17A19, 393408): <https://www.biolegend.com/en-us/products/pe-cyanine7-anti-human-cd45-recombinant-antibody-16253>
 TCR alpha/beta-BV421 (IP26, 306722): <https://www.biolegend.com/en-us/products/brilliant-violet-421-anti-human-tcr-alpha-beta-antibody-8526>

All antibodies were listed by the respective vendor as validated for flow cytometry.

Antibody validation information provided by Biolegend:

Antibody validation is a critical step in the journey towards obtaining consistent reproducibility in science. To ensure they are both specific and sensitive, we validate our antibodies through a variety of methods including:

Testing on multiple cell and tissue types with a variety of known expression levels.

Validation in multiple applications as a cross-check for specificity and to provide additional clarity for researchers.

Comparison to existing antibody clones.

Using cell treatments to modulate target expression, such as phosphatase treatment to ensure phospho-antibody specificity.

Antibody validation information provided by BD Biosciences:

Antibody specificity

BD Biosciences identifies key targets of interest in scientific research and develops its own specific antibodies or collaborates with top research scientists around the world to license their antibodies. We then transform these antibodies into flow cytometry reagents by conjugating them to a broad portfolio of high-performing dyes, including our vastly popular portfolio of BD Horizon Brilliant™ Dyes. A world-class team of research scientists helps ensure that these reagents work reliably and consistently for flow cytometry applications.

The specificity is confirmed using multiple methodologies that may include a combination of flow cytometry, immunofluorescence, immunohistochemistry or western blot to test staining on a combination of primary cells, cell lines or transfectant models.

All flow cytometry reagents are titrated on the relevant positive or negative cells. To save time and cell samples for researchers, test size reagents are bottled at an optimal concentration with the best signal-to-noise ratio on relevant models during the product development. To ensure consistent performance from lot-to-lot, each reagent is bottled to match the previous lot MFI.

Antibody validation information provided by Southern Biotech:

The success of any immunoassay hinges on the quality of the antibody reagents that are used. At SouthernBiotech, we produce all of our antibodies in-house and validate them with techniques including:

ELISA

FLISA

Flow cytometry

Western blot

Immunohistochemistry

Immunocytochemistry

Immunoprecipitation

By maintaining complete control over our antibody production workflow, we provide competitive pricing and next-day delivery, backed by fast and comprehensive technical support, giving you total confidence in your experimental results.

Validation information provided by Cell Signaling:

IKZF1 antibody: Ikaros (clone: D10E5) rabbit monoclonal antibody cat#9034: <https://www.cellsignal.com/products/primary-antibodies/ikaros-d10e5-rabbit-mab/9034>
 beta-Actin β -Actin (8H10D10) mouse monoclonal antibody cat#3700: <https://www.cellsignal.com/products/primary-antibodies/b-actin-8h10d10-mouse-mab/3700>

Kindle Biosciences:
 Digital anti mouse HRP (cat#: R1005): <https://kindlebio.com/products/29-digital-anti-mouse-hrp.html>

Eukaryotic cell lines

Policy information about [cell lines and Sex and Gender in Research](#)

Cell line source(s)	Lenti-X 293T cells were purchased from Takara (Cat#632180). Nalm6 cells were provided by Dr. Michael Milone, originally obtained from DSMZ. K562 cells were obtained from ATCC (CCL-243).
Authentication	Nalm-6 cells were periodically authenticated by flow cytometry after staining with anti-CD19 antibody. Lenti-X 293T cell were not further authenticated since they were directly obtained from the vendor. K562 cells expressing CD64 were authenticated by staining for antibodies bound to CD64.
Mycoplasma contamination	All cells were periodically tested for mycoplasma contamination. None of the cell lines were contaminated.
Commonly misidentified lines (See ICLAC register)	No commonly misidentified cell lines were used in this study

Animals and other research organisms

Policy information about [studies involving animals; ARRIVE guidelines](#) recommended for reporting animal research, and [Sex and Gender in Research](#)

Laboratory animals	NSG mice (male, 6-8 weeks) were provided by SCXC core at University of Pennsylvania. Mice were housed in a barrier facility with a 12 hour light-dark cycle at a temperature of 20-23 degrees Celsius with a humidity ranging from 30-70%.
Wild animals	No wild animals were used in this study
Reporting on sex	Only male NSG mice were used in this study.
Field-collected samples	No field-collected samples were used in this study
Ethics oversight	All studies involving animals were performed under a protocol approved by the University of Pennsylvania Institutional Animal Care and Use Committee.

Note that full information on the approval of the study protocol must also be provided in the manuscript.

Flow Cytometry

Plots

Confirm that:

- The axis labels state the marker and fluorochrome used (e.g. CD4-FITC).
- The axis scales are clearly visible. Include numbers along axes only for bottom left plot of group (a 'group' is an analysis of identical markers).
- All plots are contour plots with outliers or pseudocolor plots.
- A numerical value for number of cells or percentage (with statistics) is provided.

Methodology

Sample preparation	Sample preparation is described in the Methods.
Instrument	BD LSR II, Fortessa, or A3 Lite
Software	FlowJo (Tree Star, V10.8.1), BD FACSDiva software v8.0.1
Cell population abundance	Port-sort purity was performed by flow cytometry for one experiment and determined to be >85%.
Gating strategy	Lymphocytes and singlets were gated as shown in Ext. Data. Fig 2f for all T cell experiments. For LIPSTIC assay experiments, LIPSTIC positivity was determined as greater than the signal of CAR T cells incubated without target. Cell division was

determined by CTV dilution, with zero division signal determined by CTV-stained resting CAR T cells incubated without target.

Tick this box to confirm that a figure exemplifying the gating strategy is provided in the Supplementary Information.